CHAPTER 25
BISTATIC RADAR

Nicholas J. Willis
Technology Service Corporation

25.1 CONCEPT AND DEFINITIONS

Bistatic radar employs two sites that are separated by a considerable distance. A transmitter is placed at one site, and the associated receiver is placed at the second site. Target detection is similar to that of monostatic radar: target illuminated by the transmitter and target echoes detected and processed by the receiver. Target location is similar to but more complicated than that of a monostatic radar: total signal propagation time, orthogonal angle measurements by the receiver, and some estimate of the transmitter location are required to solve the transmitter-target-receiver triangle, called the *bistatic triangle*. Continuous-wave (CW) waveforms can often be used by a bistatic radar because site separation, possibly augmented by sidelobe cancellation, provides sufficient spatial isolation of the *direct-path* transmit signal.

When separate transmit and receive antennas are at a single site, as is common in CW radars, the term *bistatic* is not used to describe such a system since the radar has characteristics of a monostatic radar. In special cases, the antennas can be at separate sites and the radar is still considered to operate monostatically. For example, an over-the-horizon (OTH) radar can have site separation of 100 km or more. But that separation is small compared with the target location of thousands of kilometers,[1,2] and the radar operates with monostatic characteristics.

When two or more receive sites with common spatial coverage are employed and target data from each site is combined at a central location, the system is called a *multistatic radar*. Thinned, random, distorted, and distributed arrays,[3–6] interferometric radars,[7–10] the radio camera,[11,12] and the multistatic measurement system[13,14] are sometimes considered a subset of multistatic radars. They usually combine data coherently from each receiver site to form a large receive aperture. Multiple transmitters can be used with any of these configurations. They can be located at separate sites or colocated with the receive sites. Three range-only monostatic radars combined in a radar net are sometimes called a *trilateration radar*. The trilateration concept applies to multistatic radars that measure target location by time-difference-of-arrival (TDOA) or differential doppler techniques.

The foregoing definitions are broad and traditional[1,15,16] but are by no means uniformly established in the literature. Terms such as *quasi-bistatic, quasi-*

monostatic, pseudo-monostatic, tristatic, polystatic, real multistatic, multibistatic, and *netted bistatic* have also been used.[17–20] They are usually special cases of the broad definitions given above.

Passive receiving systems, or electronic support measure (ESM) systems, often use two or more receiving sites. Their purpose is typically to detect, identify, and locate transmitters such as monostatic radars. They are also called *emitter locators*. Target location is by means of combined angle measurements from each site (e.g., triangulation), TDOA, and/or differential doppler measurements between sites. These systems usually are not designed to detect and process the echoes from targets illuminated by the transmitter. They can, however, be used with a bistatic or multistatic radar to identify and locate a suitable transmitter to initialize radar operations. Thus, while they have many requirements and characteristics common to multistatic radars, they are not radars and will not be considered here.

25.2 HISTORY

Early experimental radars in the United States, the United Kingdom, France, the Soviet Union, Germany, and Japan were of the bistatic type, where the transmitter and receiver were separated by a distance comparable to the target distance.[21–26] These bistatic radars used CW transmitters and detected a beat frequency produced between the direct-path signal from the transmitter and the doppler-frequency-shifted signal scattered by a moving target. This effect was called CW wave interference.[1] The geometry was similar to that of the forward-scatter (or near-forward-scatter) configuration, where the target position is near the baseline joining transmitter and receiver. Much of the early bistatic radar technology was derived from existing communications technology—separated sites, CW transmissions, and frequencies ranging from 25 to 80 MHz.[27] These early bistatic radars were typically configured as fixed, ground-based fences to detect the *presence* of aircraft: a major, emerging threat in the 1930s. The problem of extracting target *position* information from such radars could not readily be solved with techniques available at the time.[1]

Many of the early United States bistatic radar experiments were conducted by the Naval Research Laboratory (NRL).[1] In 1922 NRL researchers detected a wooden ship using a CW wave interference radar operating at 60 MHz. An NRL proposal for further work was rejected. In 1930 an aircraft was accidentally detected when it passed through a 33-MHz direction-finding beam received by an aircraft on the ground. Interest was revived, and in 1932 CW wave interference equipment detected an aircraft up to 80 km from the transmitter. In 1934 this work was disclosed in a patent, granted to Taylor, Young, and Hyland.[21]

In the Soviet Union an operational system, the RUS-1, evolved from an experimental bistatic CW radar.[24] By the time of the German invasion in 1941, 45 systems had been built and deployed to the Far East and the Caucasus. They were subsequently replaced by the RUS-2 and RUS-2C, both pulsed radars. The RUS-2 used two trucks, one for the transmitter and one for the receiver, separated by about 300 m to provide receiver isolation. Although the RUS-2 used two sites, separation was not sufficient to define the configuration as bistatic. The French also deployed a bistatic CW radar in a two-fence con-

figuration prior to World War II, thus providing a coarse estimate of target course and speed.[24]

The Japanese deployed about 100 bistatic CW radar fences, called Type A, starting in 1941.[26] These remained in use until the end of World War II. Type A operated between 40 and 80 MHz with 3 to 400 W of transmitter power. Maximum detection ranges of up to 800 km on aircraft were achieved, with one system operating between Formosa (Taiwan) and Shanghai. Target location along the forward-scatter baseline was never achieved with this system.

A variation of these fence configurations was developed by the Germans during World War II.[17] They built a bistatic receiver, known as the Klein Heidelberg, that used a British Chain Home radar as the transmitter. The receiver gave warning of the onset of Allied bombing raids when the planes were over the English Channel, without endangering the German ground sites. This bistatic radar appears to be the first operational configuration to use a noncooperative transmitter.

The Chain Home radars themselves operated with separate transmitter and receiver sites, but again with separation small compared with target distance. However, they had a standard, reversionary mode in which, in the presence of electronic countermeasures (ECM) or a transmitter failure, a receiver site could operate with a transmitter at an adjacent site, hence becoming bistatic.[28]

The invention of the duplexer at NRL in 1936 provided a means of using pulsed waveforms with a common transmit and receive antenna. This single-site configuration is the familiar monostatic radar, and it greatly expanded the utility of radar, particularly for use by aircraft, ships, and mobile ground units. As a consequence bistatic radars became dormant.

It was not until the early 1950s that interest in bistatic radars was revived for aircraft detection.[1,29–31] The United States AN/FPS-23 was designed as a gap-filler fence for the Distant Early Warning (DEW) line in the arctic. It was installed in the mid-1950s but was later removed.[24] The Canadians also developed a bistatic radar for their McGill fence.[29,32] The United States Plato and Ordir ballistic missile detection systems were designed as the first multistatic radars; they combined range sum and doppler information from each receiver site to estimate target position. They were not deployed.[24,32]

The Azuza, Udop, and Mistram interferometeric radars, a variant of multistatic radars, were installed at the United States Eastern Test Range for precision measurement of target trajections. They used a single CW transmitter, multiple receivers at separate, precisely located sites, and cooperative beacon transponders on the target.[9,10] The SPASUR, a satellite fence interferometric radar, was also implemented with a single CW transmitter and multiple receivers but with enough performance to detect satellite-skin echoes.[7,8]

A major development at this time was the semiactive homing missile seeker, in which the large, heavy, and costly transmitter could be off-loaded from the small, expendable missile onto the launch platform (Chap. 19). While these seekers are clearly a bistatic radar configuration, missile engineers have developed a different lexicon to describe their technology and operation, e.g., semiactive versus bistatic, illuminator versus transmitter, rear reference signal versus direct-path signal, etc. The missile and radar communities continue to go their separate ways.

In the 1950s and early 1960s bistatic radar system theory was codified.[15] Bistatic radar cross-section theory was developed, and measurements were taken.[33–41] Bistatic clutter measurements were also taken.[42,43] The name *bistatic radar* was coined by K. M. Siegel and R. E. Machol in 1952.[34]

Bistatic radars received renewed interest in the 1970s and 1980s as counters to retrodirective jammers and attacks by antiradiation missiles (ARMs). Retrodirective jamming levels can be reduced by selecting a geometry such that the receive site lies outside the jammer's main beam, which is directed at the transmit site. The effectiveness of an ARM attack can be reduced by removing the transmitter from the battle area into a "sanctuary," which is less vulnerable to attack. Several air defense field test programs explored these capabilities and the problems inherent in bistatic operation, such as time synchronization, coverage, and clutter suppression.[18,44–50]

Other bistatic radar concepts were identified and tested at this time, such as *clutter tuning* from an airborne transmitter and receiver.[51–53] One potential implementation of this concept allows the receiver to generate a synthetic aperture radar (SAR) map of modest resolution directly on its velocity vector—an impossible task for the monostatic SAR. Clutter tuning combined with the sanctuary concept protects the transmitter while allowing the receiver platform to fly toward the target with no radar emissions.

The concept of using a small bistatic receiver that "hitchhikes" off airborne radars was also developed and successfully tested.[54] It alerts and cues autonomous short-range air defense and ground surveillance systems to improve survivability and acquisition performance. This hitchhiking concept was extended to other transmitters of opportunity, including a commercial television station that served as a bistatic transmitter. Initial attempts to detect aircraft were only marginally successful.[55]

Bistatic radars using space-based transmitters and receivers that are either space-based, airborne, or ground-based have been studied.[3,56–59] Limited field tests were conducted by using a communication satellite as the transmitter and a ground-based receiver to detect aircraft.[58] Since the effective radiated power of the satellite was modest and the transmitter-to-target ranges were large, detection ranges were small, <4 km, unless a very large receive aperture was used.

A pulse doppler bistatic radar was developed and tested to protect military aircraft on the ground from intruders.[60] It was configured for near-forward-scatter operation. Five small portable transmitter-receiver units, typically separated by 65 m, were located around the aircraft, with one transmitter servicing an adjacent receiver. In field tests the radar detected moving targets, including high-speed vehicles and intruders creeping at 2 cm/s.

The Multistatic Measurement System (MMS) was installed at the United States Kwajalein Missile Range in 1980 to track ballistic missile skin echoes.[14] The TRADEX L-band and ALTAIR ultrahigh-frequency (UHF) monostatic radars are used to illuminate the targets, and the bistatic echoes, collected at two unmanned stations located about 40 km from the radars, are combined coherently at a central site. The system is projected to measure three-dimensional position and velocity with accuracies better than 4 m and 0.1 m/s, respectively, throughout reentry.[13]

Other multistatic radar concepts have been studied. They include the Doppler Acquisition System (DAS), which used multiple transmitters and receivers,[61] and Distributed Array Radar (DAR) concepts, with large[3] and small[5] spatial separation between receive sites. The DAS combines data from each site noncoherently; the DAR, coherently.

Bistatic radars have been analyzed, proposed, and in some cases developed for other than military applications. Such applications include high-resolution imaging at short ranges (in the near field of the antennas) for use by robotics in an industrial environment;[62] airport ground vehicle and aircraft collision warning

and avoidance using a baseband bistatic radar;[63] planetary surface and environment measurements using a satellite-based transmitter and an earth-based receiver[64–67] or a planet-based transmitter and a satellite-based receiver;[68] geological probing of horizontally stratified, underground layers from a transmitter and receiver on the surface, usually operating at frequencies from 100 to 1000 MHz;[69] ocean wave spectral measurements (wavelength, frequency, and direction of travel) using a Loran-A system;[70] and detection and soundings of tropospheric layers, ionospheric layers, and high-altitude, clear-air atmospheric targets using ground-based sites.[16,71,72]

25.3 COORDINATE SYSTEM

A two-dimensional north-referenced coordinate system[73] is used throughout this chapter. Figure 25.1 shows the coordinate system and parameters defining bistatic radar operation in the x,y plane. This is sometimes called the *bistatic plane*.[74] The bistatic triangle lies in the bistatic plane. The distance L between the transmitter and the receiver is called the *baseline range* or simply the *baseline*. The angles θ_T and θ_R are, respectively, the transmitter and receiver look angles. They are also called angles of arrival (AOA) or lines of sight (LOS). Note that the bistatic angle $\beta = \theta_T - \theta_R$. It is also called the cut angle or the scattering angle. It is convenient to use β in calculations of target-related parameters and θ_T or θ_R in calculations of transmitter- or receiver-related parameters. Development of three-dimensional bistatic coordinate systems for some applications is available elsewhere.[16,46,48,75,76]

A useful relationship is that the bisector of the bistatic angle is orthogonal to

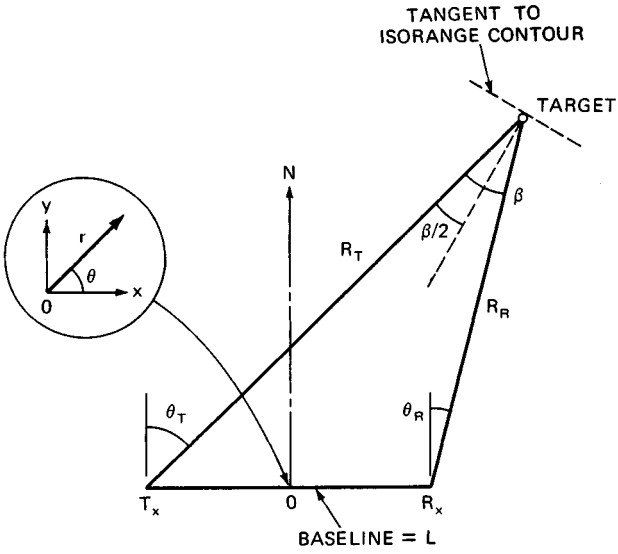

FIG. 25.1 Bistatic radar north coordinate system for two dimensions.[73]

the tangent of an ellipse with foci at the transmitter and receiver sites and passing through the target position. Such an ellipse is called an *isorange contour*. The tangent is often a good approximation to an isorange contour within the bistatic footprint, the area common to the transmit and receive beams.

Geometry often distinguishes bistatic from monostatic radar operation. In these distinguishing cases, equivalent monostatic operation is obtained by setting $L = O$, or $R_T = R_R$ and $\beta = 0$.

25.4 RANGE RELATIONSHIPS

Range Equation.[1,3,5,15,16,77,78] The range equation for a bistatic radar is derived in a manner completely analogous to that for a monostatic radar. With this analog, the bistatic radar maximum-range equation can be written as

$$(R_T R_R)_{\max} = \left(\frac{P_T G_T G_R \lambda^2 \sigma_B F_T^2 F_R^2}{(4\pi)^3 K T_s B_n (S/N)_{\min} L_T L_R} \right)^{1/2} \tag{25.1}$$

where R_T = transmitter-to-target range
R_R = receiver-to-target range
P_T = transmitter power
G_T = transmit antenna power gain
G_R = receive antenna power gain
λ = wavelength
σ_B = bistatic radar target cross section
F_T = pattern propagation factor for transmitter-to-target path
F_R = pattern propagation factor for target-to-receiver path
K = Boltzmann's constant
T_s = receive system noise temperature
B_n = noise bandwidth of receiver's predetection filter
$(S/N)_{\min}$ = signal-to-noise power ratio required for detection
L_T = transmit system losses (> 1) not included in other parameters
L_R = receive system loss (> 1) not included in other parameters

Equation (25.1) is related to the corresponding monostatic radar range equation by the following: $\sigma_M = \sigma_B$, $L_T L_R = L_M$, and $R_T^2 R_R^2 = R_M^4$. More specific formulations of the maximum-range equation, as given in Chap. 2, also apply to the bistatic radar case. Equation (25.1) is used in this chapter because it more clearly illustrates the utility of constant S/N contours (ovals of Cassini) and other geometric relationships. The right side of Eq. (25.1) is called the bistatic maximum-range product κ.

Ovals of Cassini. Equation (25.1), with $(R_T R_R)_{\max} = \kappa$, is the maximum-range oval of Cassini. It can be used to estimate the signal-to-noise S/N power ratio at any R_T and R_R simply by dropping the "max" and "min" designation for $(R_T R_R)$ and S/N respectively. Then when Eq. (25.1) is solved for S/N,

$$S/N = \frac{k}{R_T^2 R_R^2} \tag{25.2}$$

where S/N = signal-to-noise power ratio at ranges R_T, R_R, and

$$k = \frac{P_T G_T G_R \lambda^2 \sigma_B F_T^2 F_R^2}{(4\pi)^3 K T_S B_n L_T L_R} \tag{25.3}$$

The term k is the bistatic radar constant. The constants k and κ are related as

$$k = \kappa^2 (S/N)_{\min} \tag{25.4}$$

Equation (25.2) represents one form of the ovals of Cassini. They can be plotted on the bistatic plane when R_T and R_R are converted to polar coordinates (r,θ), as shown on Fig. 25.1:

$$R_T^2 R_R^2 = (r^2 + L^2/4)^2 - r^2 L^2 \cos^2 \theta \tag{25.5}$$

where L is the baseline range. Figure 25.2 is such a plot for k arbitrarily set to $30L^4$.

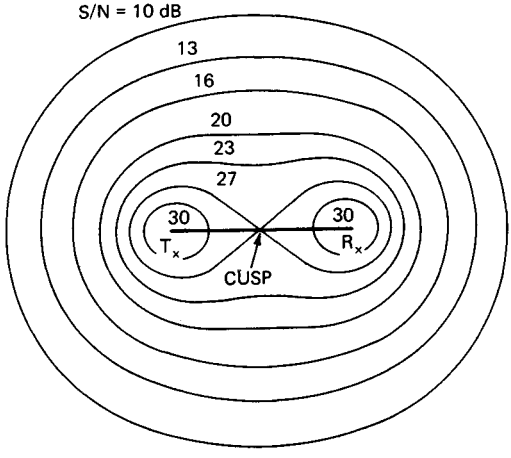

FIG. 25.2 Contours of constant signal-to-noise ratio, or ovals of Cassini, where the baseline = L and $k = 30L^4$.

The ovals of Fig. 25.2 are contours of constant signal-to-noise ratio on any bistatic plane. They assume that an adequate line of sight (LOS) exists on the transmitter-to-target path and the receiver-to-target path and that σ_B, F_T, and F_R are invariant with r and θ, which is usually not the case. But this simplifying assumption is useful in understanding basic relationships and constraints. As S/N or L increases, the ovals shrink, finally collapsing around the transmitter and receiver sites. The point on the baseline where the oval breaks into two parts is called the cusp. The oval is called a lemniscate (of two parts) at this S/N. When $L = 0$, $R_T R_R = r^2$, which is the monostatic case where the ovals become circles.

Operating Regions. Ovals of Cassini define three distinct operating regions for a bistatic radar: receiver-centered region, transmitter-centered region, and receiver-transmitter-centered region, or simply the cosite region. Critical to the selection of these operating regions is the value of the bistatic radar constant k that is available. Many of the terms in Eq. (25.3) are transmitter-controlled. It is convenient to define three transmitter configurations that control k: dedicated, cooperative, and noncooperative. The *dedicated* transmitter is

defined as being under both design and operational control of the bistatic radar system; the *cooperative* transmitter is designed for other functions but found suitable to support bistatic operations and can be controlled to do so; and the *noncooperative* transmitter, while suitable for bistatic operations, cannot be controlled. The bistatic receiver is sometimes said to hitchhike off a cooperative or noncooperative transmitter, usually a monostatic radar.

Table 25.1 summarizes useful bistatic radar applications permitted by operating regions and transmitter configurations. The two omitted entries on the "Transmitter-centered" row are operational constraints: a dedicated or cooperative transmitter can usually gather nearby data in a monostatic radar mode more easily than can a remote, bistatic receiver. The two omitted entries on the "Cosite" row are technical constraints: to generate a sufficiently large bistatic radar constant for cosite operation the transmitter design and operation must be optimized for bistatic radar use; hence the dedicated transmitter is often the only viable cosite configuration. Exceptions to this rule include exploiting HF groundwave propagation and occasional atmospheric ducting.

Isorange Contours. The transmitter-to-target-to-receiver range measured by a bistatic radar is the sum $(R_T + R_R)$. This sum locates the target somewhere on the surface of an ellipsoid whose two foci are the transmitter and receiver

TABLE 25.1 Bistatic Radar Applications

Bistatic radar operating regions	Range relationships	Transmitter configuration		
		Dedicated	Cooperative	Noncooperative
Receiver-centered	$R_T \gg R_R$ k small	• Air-to-ground attack (silent penetration) • Semiactive homing missile (lock on after launch)	• Short-range air defense • Ground surveillance • Passive situation awareness	• Passive situation awareness
Transmitter-centered	$R_R \gg R_T$ k small	. . . . .	. . . . .	• Intelligence data gathering • Missile launch alert
Cosite	$R_T \sim R_R$ k larger	• Medium-range air defense • Satellite tracking • Range instrumentation • Semiactive homing missile (lock on before launch) • Intrusion detection	. . . . .	. . . . .

sites. The intersection of the bistatic plane and this ellipsoid produces the familiar ellipses of constant range sum, or *isorange contours*.

Since the (constant range sum) isorange contours and the (constant *S/N*) ovals of Cassini are not colinear, the target's *S/N* will vary for each target position on the isorange contour. This variation can be important when target returns are processed over a bistatic range cell, defined by two concentric isorange contours with separation $\Delta R_B \approx c\tau/2 \cos(\beta/2)$, where τ = compressed pulse width. The *S/N* over an isorange contour, $(S/N)_i$ is

$$(S/N)_i = \frac{4k(1 + \cos\beta)^2}{[(R_T + R_R)^2 - L^2]^2} \tag{25.6}$$

where the denominator defines the isorange countour and the bistatic angle β defines the target's position on the isorange contour.

The maximum bistatic angle, β_{max}, on an isorange contour is $2\sin^{-1}[L/(R_T + R_R)]$, where $L/(R_T + R_R)$ is the eccentricity of the isorange contour. The minimum bistatic angle, β_{min}, is zero for all isorange contours. For example, when $L/(R_T + R_R)] = 0.95$, $\beta_{max} = 143.6°$ and $(S/N)_i$ at β_{max} is 20 dB less than at β_{min}.

25.5 AREA RELATIONSHIPS

Location.[1,15,16,18,46–48,73,79–83] Target position relative to the receive site (θ_R, R_R) is usually required in a bistatic radar. The receiver look angle θ_R is measured directly, or target azimuth and elevation measurements are converted directly to θ_R. Beam-splitting techniques can be used to increase the measurement accuracy.

The receiver-to-target range R_R cannot be measured directly, but it can be calculated by solving the bistatic triangle (Fig. 25.1). A typical solution in elliptical coordinates is[1]

$$R_R = \frac{(R_T + R_R)^2 - L^2}{2(R_T + R_R + L \sin\theta_R)} \tag{25.7}$$

The baseline L can be calculated from coordinates provided by a dedicated transmitter or measured by an emitter location system. The range sum $(R_T + R_R)$ can be estimated by two methods. In the direct method the receiver measures the time interval ΔT_{rt} between reception of the transmitted pulse and reception of the target echo. It then calculates the range sum as $(R_T + R_R) = c\Delta T_{rt} + L$. This method can be used with any transmitter configuration, given an adequate LOS between transmitter and receiver.

In the indirect method synchronized stable clocks are used by the receiver and (dedicated) transmitter. The receiver measures the time interval ΔT_{tt} between transmission of the pulse and reception of the target echo. It then calculates the range sum as $(R_T + R_R) = c\Delta T_{tt}$. A transmitter-to-receiver LOS is not required unless periodic clock synchronization is implemented over the direct path.

For the special case of a bistatic radar using the direct range sum estimation method, where $L \gg c\Delta T_{rt}$, Eq. (25.7) can be approximated as

$$R_R = \frac{c\Delta T_{rt}}{1 + \sin \theta_R} \tag{25.8}$$

This approximation does not require an estimate of L. The error in Eq. (25.8) is less than 10 percent for $0° < \theta_R < 180°$ and $L > 4.6\, c\Delta T_{rt}$.

Other target location techniques are possible.[16,18] The transmitter beam-pointing angle θ_T can be used in place of θ_R. Unless the transmitter is also a monostatic radar tracking the target, target location accuracy is degraded, since beam splitting is sacrificed. A hyperbolic measurement system can be used, in which a receiver measures the difference in propagation times from two separate transmitters. The locus of target position now lies on a hyperbola, and the intersection of the receiver's AOA (angle of arrival) estimate with the hyperbola establishes the target position. Use of a third transmitter provides a full hyperbolic fix on the target. A theta-theta location technique uses the angles θ_T and θ_R and an estimate of L, where θ_T is typically provided by a monostatic radar, which acts as a cooperative bistatic transmitter.

For an elliptic location system, target location errors typically *increase* as the target approaches the baseline, ignoring S/N changes. The principal source of errors is the geometry inherent in Eq. (25.7). Additional errors occur when the direct range sum estimation method is used. They include interference from the direct-path signal (analogous to eclipsing), pulse instability, and multipath effects. Compounding the eclipsing problem is interference from range sidelobes when pulse compression is used by the transmitter. If linear FM pulse compression is used, Hamming or cosine-squared time-domain weighting by the receiver improves near-in sidelobe suppression by about 5 dB, when compared with the same type of frequency-domain weighting.[79]

For a hyperbolic location system, target location errors *decrease* as the target approaches the line joining the two transmitters. For a theta-theta location system, the error is a minimum when the target lies on the perpendicular bisector of the baseline with $\beta = 45°$ and increases elsewhere.[18] When successive data measurements (or redundant data) are available to a bistatic or multistatic radar, target state estimates can be made with Kalman or other types of filters.[80,81]

Coverage. Bistatic radar coverage, like monostatic radar coverage, is determined by both sensitivity and propagation. Bistatic radar sensitivity is set by the contour of constant $(S/N)_{\min}$ and the oval of Cassini. Bistatic radar propagation requires a suitable path between the target and both sites and must include the effects of multipath, diffraction, refraction, shadowing, absorption, and geometry. The first five effects are usually included in the pattern propagation and loss factor terms of Eq. (25.1). The geometry effect is treated separately.

For given target, transmitter, and receiver altitudes the target must simultaneously be within LOS to both the transmitter and the receiver sites. For a smooth earth these LOS requirements are established by coverage circles centered at each site. Targets in the area common to both circles have an LOS to both sites as shown in Fig. 25.3. For a 4/3 earth model, the radius of these coverage circles, in kilometers, is approximated by[16]

$$r_R = 130(\sqrt{h_t} + \sqrt{h_R}) \tag{25.9}$$

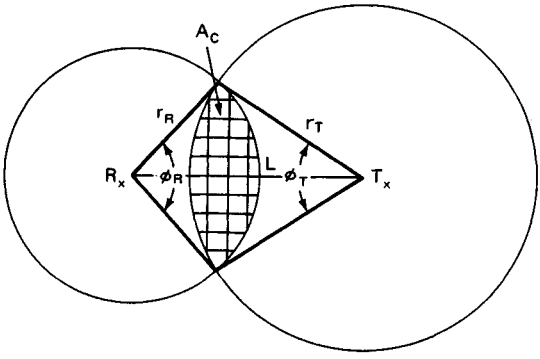

FIG. 25.3 Geometry for common-coverage area A_C.

$$\text{and } r_T = 130(\sqrt{h_t} + \sqrt{h_T}) \tag{25.10}$$

where h_t = target altitude, km
h_R = receive antenna altitude, km
h_T = transmit antenna altitude, km

If the receiver establishes synchronization via the direct-path link, then an adequate LOS is also required between transmitter and receiver. In this case $h_t = 0$ and $r_R + r_T \geq L$, where L is the baseline range. Thus,

$$L \leq 130(\sqrt{h_R} + \sqrt{h_T}) \tag{25.11}$$

If synchronization is accomplished by stable clocks, this LOS is not required and the system must satisfy only the requirements of Eqs. (25.9) and (25.10).

The common-coverage area A_C is shown in Fig. 25.3 as the intersection of the two coverage circles and is

$$A_C = \tfrac{1}{2}[r_R^2(\phi_R - \sin \phi_R) + r_T^2(\phi_T - \sin \phi_T)] \tag{25.12}$$

where ϕ_R and ϕ_T are shown on Fig. 25.3 and are

$$\phi_R = 2 \cos^{-1}\left(\frac{r_R^2 - r_T^2 + L^2}{2r_R L}\right) \tag{25.13}$$

$$\phi_T = 2 \cos^{-1}\left(\frac{r_T^2 - r_R^2 + L^2}{2r_T L}\right) \tag{25.14}$$

Terrain and other types of masking or shadowing degrade both monostatic and bistatic coverage. For ground-based bistatic transmitters and receivers the degradation can be severe.[84] For this reason some air defense bistatic radar concepts use an elevated or airborne transmitter.[44,45,48,54] As a general rule bistatic coverage is less than monostatic coverage in both single and netted configurations.

Clutter Cell Area.[42,51,59,73,85–89] The main-lobe bistatic clutter cell area A_c is defined, in the broadest sense, as the intersection of the range resolution cell, the doppler resolution cell, and the bistatic main-beam footprint. The range and doppler resolution cells are defined by isorange and isodoppler contours, respectively. The bistatic footprint is the area on the ground, or clutter surface, common to the one-way transmit and receive beams, where the beamwidths are conventionally taken at the 3-dB points. Three clutter cell cases are usually of interest: beamwidth-limited, range-limited, and doppler-limited.

Beamwidth-Limited Clutter Cell Area. The beamwidth-limited clutter cell area $(A_c)_b$ is the bistatic footprint. It has been evaluated for specific antenna pattern functions and specific geometries by numerical integration techniques.[42,85,86] At small grazing angles a two-dimensional approximation to $(A_c)_b$ is a parallelogram shown as the single-hatched area in Fig. 25.4 with area

$$(A_c)_b = \frac{R_R \Delta\theta_R R_T \Delta\theta_T}{\sin\beta} \tag{25.15}$$

where $R_R\ \Delta\theta_R$ is the cross-range dimension of the receive beam at the clutter cell, $R_T\ \Delta\theta_T$ is the corresponding dimension for the transmit beam, and $\Delta\theta_R$ and $\Delta\theta_T$ are, respectively, the 3 dB beamwidth of the receive and transmit beams. Respective transmit and receive beam rays are assumed to be parallel, which is a reasonable approximation when the range sum is much greater than the baseline range, $R_T + R_R >> L$. The cell area is a minimum at $\beta = 90°$.

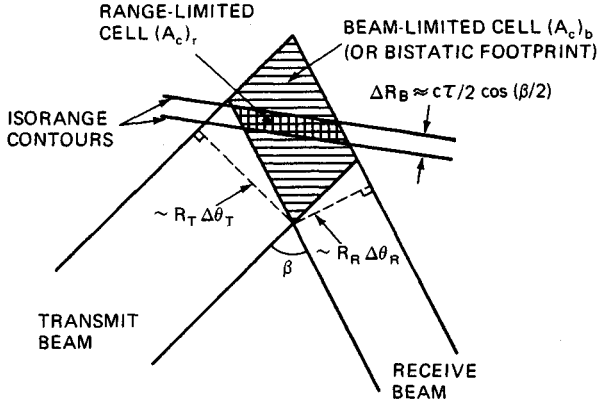

FIG. 25.4 Geometry for clutter cell areas.

Range-Limited Clutter Cell Area. The range-limited clutter cell area $(A_c)_r$ has been evaluated at small grazing angles for all geometries of interest.[87] At small grazing angles and at large range sums ($R_T + R_R >>$ L), a two-dimensional approximation to $(A_c)_r$ is a parallelogram shown as the double-hatched area in Fig. 25.4 with area

$$(A_c)_r = \frac{c\tau R_R \Delta\theta_R}{2\cos^2(\beta/2)} \tag{25.16}$$

where τ is the radar's compressed pulse width. The isorange contours are assumed to be straight lines within the bistatic footprint. For this example the

cross-range dimension of the transmit beam $R_T\Delta\theta_T$ is greater than that of the receive beam $R_R\Delta\theta_R$, so that the clutter cell is determined by the intersection of the receive beam and the range cell. For a given geometry one or the other beam will usually determine the clutter cell area. In either case the cell area increases as β increases. For small range sums, the cell shape is trapezoidal or triangular at small β and is rhomboidal or hexagonal at large β.[87]

An exact expression for $(A_c)_r$ has been developed,[88] again for two dimensions, with one beam and the range cell determining the clutter cell area. Equation (25.16) gives results that are within a few percent of the exact results for $\beta < 90°$. The error increases significantly for $\beta \gg 90°$ and $\theta_R < -80°$.

Doppler-Limited Clutter Cell Area. The doppler-limited clutter cell area $(A_c)_d$ has been determined by numerical integration techniques when it is bounded by a range resolution cell.[51,89] No convenient algebraic expression has been developed for the cell area since the doppler cell size and orientation with respect to the baseline change as the transmitter and receiver velocity vectors and look angles change. In the special case where the transmitter and receiver velocity vectors are equal and the bistatic angle is large, the isorange and isodoppler contours are essentially parallel, creating very large clutter cell areas.[59]

25.6 DOPPLER RELATIONSHIPS

Figure 25.5 defines the geometry and kinematics for bistatic doppler when the target, transmitter, and receiver are moving. The target has a velocity vector of magnitude V and aspect angle δ referenced to the bistatic bisector. The transmitter and receiver have velocity vectors of magnitude V_T and V_R and aspect angles δ_T and δ_R referenced to the north coordinate system of Fig. 25.1, respectively.

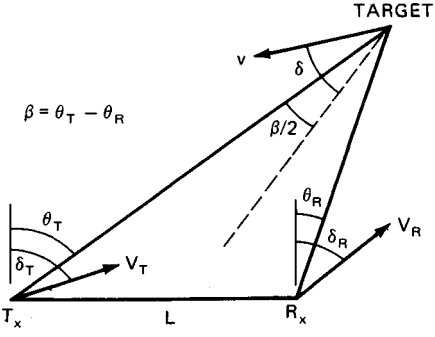

FIG. 25.5 Geometry for bistatic doppler.

Target Doppler. When the transmitter and receiver are stationary ($V_T = V_R = 0$), the target's bistatic doppler at the receive site f_B is

$$f_B = (2V/\lambda)\cos\delta\cos(\beta/2) \tag{25.17}$$

When $\beta = 0°$, Eq. (25.17) reduces to the monostatic case, where δ is now the angle between the velocity vector and the radar-to-target LOS, which is colinear

with the bistatic bisector. When $\beta = 180°$, the forward-scatter case, $f_B = 0$ for any δ. Equation (25.17) shows that:

- For a given δ, the magnitude of the bistatic target doppler is never greater than that of the monostatic target doppler when the monostatic radar is located on the bistatic bisector.
- For all β, when $-90° < \delta < +90°$, the bistatic doppler is positive; under this definition a closing target referenced to the bistatic bisector generates a positive, or *up*, doppler.
- For all β, when the target's velocity vector is normal to the bistatic bisector ($\delta = \pm 90°$) the bistatic doppler is zero; the vector is tangent to a range-sum ellipse drawn through the target position (a contour of zero target doppler).
- For all $\beta < 180°$, when the target's velocity vector is colinear with the bistatic bisector, the magnitude of the bistatic doppler is maximum; the vector is also tangent to an orthogonal hyperbola drawn through the target position, which is a contour of maximum target doppler.

Isodoppler Contours. When the target is stationary and the transmitter and receiver are moving (e.g., airborne), the bistatic doppler shift at the receiver site f_{TR} is

$$f_{TR} = (V_T/\lambda) \cos (\delta_T - \theta_T) + (V_R/\lambda) \cos (\delta_R - \theta_R) \tag{25.18}$$

where the terms are defined on Fig. 25.5.

The locus of points for constant doppler shift on the earth's surface is called an *isodoppler contour*, or *isodop*. In the monostatic case and a flat earth, these isodops are conic sections in three dimensions and radial lines emanating from the radar in two dimensions. In the bistatic case the isodops are skewed, depending upon the geometry and kinematics. They are developed analytically for two dimensions and a flat earth by setting f_{TR} = constant in Eq. (25.18) and solving for θ_R (or θ_T if appropriate).

Figure 25.6 is a plot of bistatic isodops in a two-dimensional bistatic plane, i.e., where the transmitter and receiver are at zero or near-zero altitude, for the following conditions:[90]

$$\begin{aligned} V_T = V_R &= 250 \text{ m/s} \\ \delta_T &= 0° \\ \delta_R &= 45° \\ \lambda &= 0.03 \text{ m} \end{aligned}$$

The dimension of the grid on the bistatic plane is arbitrary; that is, the isodops are invariant with scale. On the left and right sides of Fig. 25.6 the isodops approximate radial lines, which are pseudo-monostatic operating points.

25.7 TARGET CROSS SECTION[1,16,33–41,91–102,104,105]

The bistatic radar cross section (RCS) of a target σ_B is a measure, as is the monostatic radar cross section σ_M, of the energy scattered from the target in the

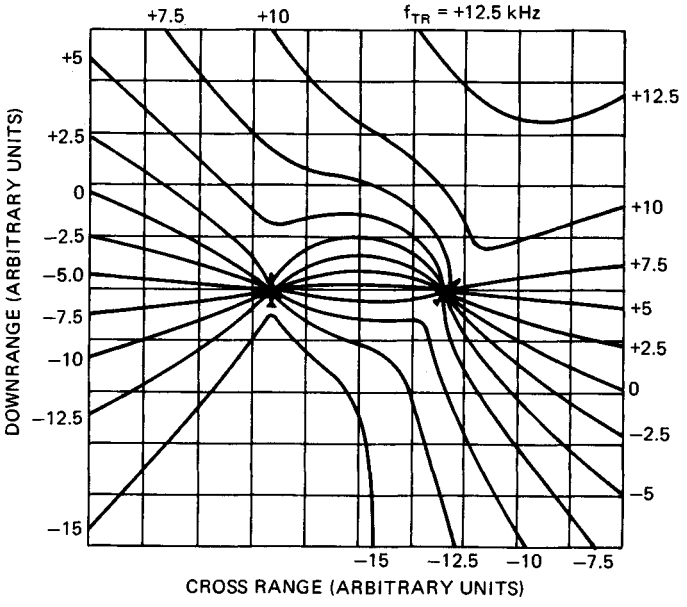

FIG. 25.6 Bistatic isodoppler contours for two dimensions and a flat earth.[90]

direction of the receiver. Bistatic cross sections are more complex than monostatic cross sections since σ_B is a function of aspect angle and bistatic angle.

Three regions of bistatic RCS are of interest: pseudo-monostatic, bistatic, and forward scatter (sometimes called near-forward scatter[99]). Each region is defined by the bistatic angle. The extent of each region is set primarily by physical characteristics of the target.

Pseudo-Monostatic RCS Region. The Crispin and Siegal monostatic-bistatic equivalence theorem applies in the pseudo-monostatic region:[36] for vanishingly small wavelengths the bistatic RCS of a sufficiently smooth, perfectly conducting target is equal to the monostatic RCS measured on the bisector of the bistatic angle. Sufficiently smooth targets typically include spheres, elliptic cylinders, cones, and ogives. Figure 25.7 shows the theoretical bistatic RCS of two perfectly conducting spheres as a function of bistatic angle.[1,92–95] For the larger sphere (near the optics region) the pseudo-monostatic region extends to $\beta = \sim 100°$, with an error of 3 dB. And even for the smaller sphere (in the resonance region) the pseudo-monostatic region extends to $\beta = \sim 40°$. Measurements[38] of a sphere with $a = 0.42\ \lambda$, where a is the sphere radius, match within 3 dB the values for the smaller sphere in Fig. 25.7.

For targets of more complex structure, the extent of the pseudo-monostatic region is considerably reduced. A variation of the equivalence theorem developed by Kell[41] applies to this case: for small bistatic angles, typically less than 5°, the bistatic RCS of a complex target is equal to the monostatic RCS measured on the bisector of the bistatic angle at a frequency lower by a factor of cos (β/2).

Kell's complex targets are defined as an assembly of discrete scattering cen-

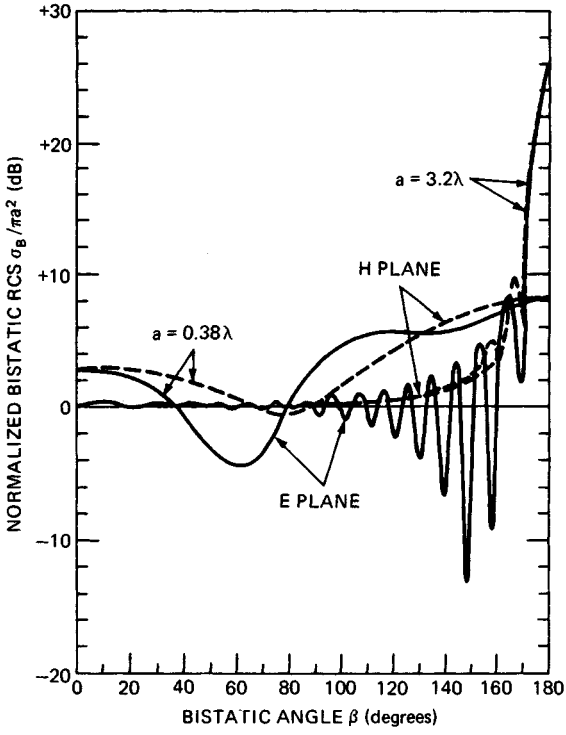

FIG. 25.7 Theoretical bistatic RCS for two perfectly conducting spheres, where a = sphere radius and λ = wavelength.[1,92–95]

ters (simple centers such as flat plates, reflex centers such as corner reflectors, skewed reflex centers such as a dihedral with corner $\neq 90°$ and stationary phase regions for creeping waves). When the wavelength is small compared with the target dimensions, these complex target models approximate many aircraft, ships, ground vehicles, and some missiles. The targets can be composed of conducting and dielectric materials.

The cos ($\beta/2$) frequency reduction term has little effect in Kell's pseudomonostatic region, $0 < \beta < \sim 5°$, since a 5° bistatic angle corresponds to less than 0.1 percent shift in wavelength. At $\beta > 5°$ the change in radiation properties from discrete scattering centers is likely to dominate any cos ($\beta/2$) frequency reduction effect.[41] Thus the cos ($\beta/2$) term is often ignored.

Both versions of the equivalence theorem are valid when the positions of the transmitter and receiver are interchanged, given that the target-scattering media are reciprocal. Most media are reciprocal. Exceptions are gyrotropic media, such as ferrite materials and the ionosphere.[103]

Whenever the equivalence theorem is valid, Kell[41] provides a simple method for deriving bistatic RCS data from monostatic RCS data when plotted as a function of target aspect angle. Bistatic RCS data for the same polarization is obtained by translating along the target aspect angle axis by one-half of the desired bistatic angle. If monostatic RCS data is also available as a function of frequency, the monostatic curve for f sec ($\beta/2$), where f is the bistatic frequency, is used to

estimate the bistatic RCS at f. As outlined earlier, this correction is usually small.

Bistatic RCS Region. The bistatic angle at which the equivalence theorem fails to predict the bistatic RCS identifies the start of the second, bistatic region. In this region the bistatic RCS diverges from the monostatic RCS. Kell[41] identified three sources of this divergence for complex targets and for a target aspect angle fixed with respect to the bistatic bisector. These sources are (1) changes in relative phase between discrete scattering centers, (2) changes in radiation from discrete scattering centers, and (3) changes in the existence of centers—appearance of new centers or disappearance of those previously present.

The first source is analogous to fluctuations in monostatic RCS as the target aspect angle changes, but now the effect is caused by a change in bistatic angle.[104] The second source occurs when, for example, the discrete scattering center reradiates, i.e., retroreflects, energy toward the transmitter and the receiver is positioned on the edge of or outside the retroflected beamwidth; thus the received energy is reduced. The third source is typically caused by shadowing, for example, by an aircraft fuselage blocking one of the bistatic paths—transmitter or receiver LOS to a scattering center.

In general, this divergence results in a bistatic RCS lower than the monostatic RCS for complex targets. Exceptions include (1) some target aspect angles that generate a low monostatic RCS and a high bistatic specular RCS at specific bistatic angles, (2) targets that are designed for low monostatic RCS over a range of aspect angles, and (3) shadowing that sometimes occur in a monostatic geometry and not in a bistatic geometry.[92]

Ewell and Zehner[97] measured the monostatic and bistatic RCS of coastal freighters at X band when both the transmitter and the receiver were near grazing incidence. The data was plotted as a ratio of bistatic to monostatic RCS, σ_B/σ_M. The measurements match Kell's model: of the 27 data points, 24 show bistatic RCS lower than monostatic RCS. The bistatic RCS reduction starts at about $\beta = 5°$ and trends downward to $\sigma_B/\sigma_M \simeq -15$ dB at $\beta \simeq 50°$. Most of the data points are in the region $5° < \beta < 30°$ where $-2 \text{ dB} > \sigma_B/\sigma_M > -12$ dB.

Glint Reduction in the Bistatic RCS Region. A second effect can occur in the bistatic region. When the bistatic RCS reduction is caused by a loss or attenuation of large discrete scattering centers, for example through shadowing, target glint is often reduced. Target glint is the angular displacement in apparent phase center of a target return and is caused by the phase interference between two or more dominant scatters within a radar resolution cell. As the target aspect angle changes, the apparent phase center shifts, often with excursions beyond the physical extent of the target. These excursions can significantly increase the errors in angle tracking or measurement systems. When the returns from dominant scatterers are reduced in the bistatic region, the source and hence the magnitude of glint excursions are reduced. Limited measurements for tactical aircraft show that, for a 30° bistatic angle, peak glint excursions can be reduced by a factor of 2 or more, with most of the excursions contained within the physical extent of the target.[54]

Forward-Scatter RCS Region. The third bistatic RCS region, forward scatter, occurs when the bistatic angle approaches 180°. When $\beta = 180°$, Siegel[33] showed, based on physical optics, that the forward-scatter RCS, σ_F, of

a target with silhouette (or shadow) area A is $\sigma_F = 4\pi A^2/\lambda^2$, where λ, the wavelength, is small compared with the target dimensions. The targets can be either smooth or complex structures and, from the application of Babinet's principle, can be totally absorbing.[37,91]

For $\beta < 180°$, the forward-scatter RCS rolls off from σ_F. The rolloff is approximated by treating the shadow area A as a uniformly illuminated antenna aperture. The radiation pattern of this *shadow aperture* is equal to the forward-scatter RCS rolloff when $(\pi - \beta)$ is substituted for the angle off the aperture normal. A sphere of radius a will roll off 3 dB at $(\pi - \beta) \simeq \lambda/\pi a$, when $a/\lambda \gg 1$.[15] Although the $a/\lambda \gg 1$ criterion is not satisfied in Fig. 25.7, the curve for $a = 3.2\lambda$ still exhibits this phenomenon: 3 dB reduction in σ_F at $\beta \simeq 174°$. (The value of σ_F at $\beta = 180°$ also matches $4\pi A^2/\lambda^2$ within 1 dB.) Figure 25.7 shows the rolloff approximating $J_0(x)/x$ down to $\beta \simeq 130°$, where J_0 is a Bessel function of zero order. A linear aperture of length D, with aspect angle orthogonal to the transmitter LOS, will roll off 3 dB at $(\pi - \beta) = \lambda/2D$, where $D/\lambda \gg 1$. The forward-scatter RCS rolloff continues, with sidelobes approximating $\sin x/x$ over the forward-scatter quadrant ($\beta > 90°$).[105] For other aspect angles and targets with complex shadow apertures, calculation of the forward-scatter RCS rolloff usually requires computer simulation.

The forward-scatter RCS of more complex bodies has been simulated and measured; the bodies were both reflecting and absorbing.[34,37,38,92,98,100–102] Paddison et al.[100] report both measurements and calculations via computer simulation of forward-scatter RCS for a right circular aluminum cylinder at 35 GHz and bistatic angles up to 175.4°. Calculations were made via the method of moments,[106] and measurements were made by Delco.[98] A good match between measurements and calculations was obtained for targets with dimensions of the order of several wavelengths. A similar match to Delco measurements was obtained by Cha et al., using physical-theory-of-diffraction methods for targets that are larger than several wavelengths and the method of moments otherwise.[102]

Figure 25.8 shows calculations of a 16- by 1.85-cm cylinder with 992 facets at 35 GHz, for three fixed transmitter-to-target geometries: (*a*) near end on, (*b*) 45° aspect angle, and (*c*) broadside.[100] The broadside geometry shows the classic forward-scattering lobe from a rectangular aperture, with approximate $\sin x/x$ sidelobe rolloff out to $\beta \simeq 110°$. The three bistatic RCS regions are quite distinct: pseudomonostatic at $\beta < 20°$, bistatic at $20° < \beta < 140°$, and forward scatter at $\beta > 140°$. The other two geometries show a similar but broader forward-scatter lobe, as is expected since the silhouette area and hence the shadowing aperture are smaller. The 45° aspect geometry is of interest because the RCS in the bistatic region is larger than the monostatic RCS for most bistatic angles. The large spike at $\beta = 90°$ is the bistatic specular lobe, analogous to the monostatic specular lobe in the broadside geometry. While Fig. 25.8 shows the clear dependency of bistatic RCS on both aspect and bistatic angle, it also serves to caution attempts to use oversimplified bistatic RCS models, especially in the bistatic region.

25.8 CLUTTER

The bistatic radar cross section of clutter σ_c is a measure, as is the monostatic radar clutter cross section, of the energy scattered from a clutter cell area A_c in the direction of the receiver. It is defined as $\sigma_c = \sigma_B{}^0 A_c$, where $\sigma_B{}^0$ is the scattering coefficient, or the clutter cross section per unit area of the illuminated sur-

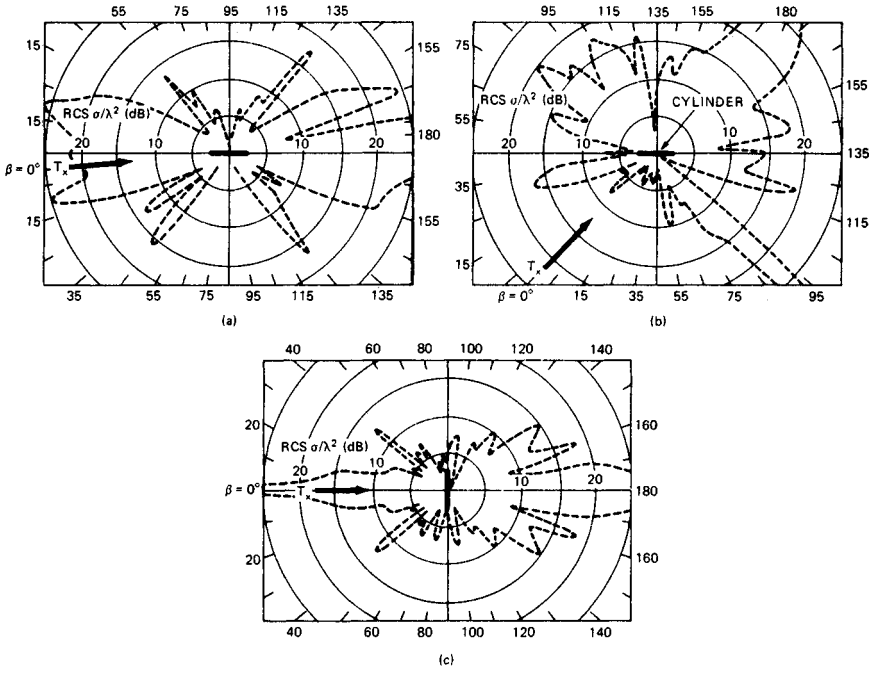

FIG. 25.8 Calculated bistatic RCS, replotted as a function of bistatic angle for a conducting cylinder, 16 by 1.85 cm at 35 GHz, *HH* polarization.[100] (*a*) Near end on. (*b*) 45° aspect angle. (*c*) Broadside.

face. The clutter cell area is given for beam- and range-limited cases in Sec. 25.5. This section considers measured and estimated values of σ_B^0, which vary as a function of the surface composition, frequency, and geometry. And, in contrast to the monostatic case, little measured data for σ_B^0 has been reported.[42,43,107–115]

The available database for terrain and sea clutter at microwave frequencies consists of six measurement programs, which are summarized in Table 25.2. The measurement angles shown in Table 25.2 are defined in Fig. 25.9, which is a clutter-centered coordinate system similar to those used in all the measurement programs. Because terrain and sea are reciprocal media, θ_i and θ_s are interchangeable in the subsequent data.[103] The Pidgeon data was analyzed by Domville[109] and Nathanson.[116] Vander Schurr and Tomlinson[117] analyzed the Larson and Cost data.

In addition to this database, bistatic reflectivity measurements have been made at optical[118] and sonic[119] wavelengths and of buildings,[120] airport structures,[121] and planetary surfaces.[66,122] In each of these measurements, the reflectivity data is expressed in terms of reflected power, not σ_B^0.[103]

The bistatic angle is calculated from the angles in Fig. 25.9 by the use of direction cosines:

$$\beta = \cos^{-1} (\sin \theta_i \sin \theta_s - \cos \theta_i \cos \theta_s \cos \phi) \tag{25.19}$$

TABLE 25.2 Summary of Measurement Programs for Bistatic Scattering Coefficient, σ_B^0

Reference (date)	Organization	Author	Surface composition	Frequency	Polarization	Measurement angles (degrees)		
						θ_i	θ_s	ϕ
42 (1965)	Ohio State University (Antenna Laboratory)	Cost, Peake	Smooth sand	10 GHz	*VV, HH, HV*	5–30, 10–70	5–30, 5–90	0–145, 0, 180
			Loam					
			Soybeans					
			Rough sand	10 GHz	*VV, HH, HV*	5–70	5–90	0–180
			Loam with stubble					
			Grass					
43 (1966)	Johns Hopkins University (APL)	Pidgeon	Sea (sea states 1, 2, 3)	C band	*VV, VH*	0.2–3	10–90	180
107 (1967)			Sea (Beaufort, wind 5)	X band	*HH*	1–8	12–45	180
108 (1967)	GEC (Electronics) Ltd., England	Domville	Rural land	X band	*VV, HH*	6–90*	6–180*	180, 165
			Urban land					
			Sea (20-kn wind)					
109 (1968)			Sea (20-kn wind)	X band	*VV, HH*	~ 0–90*	~ 0–180*	180, 165
110 (1969)			Semidesert	X band	*VV, HH*	~ 0	?	180, 165
111 (1977) 112 (1978)	University of Michigan (ERIM)	Larson, Heimiller	Grass with cement taxiway	1.3 and 9.4 GHz	*HH, HV*	10, 40	5, 10, 20	0–180
			Weeds and scrub trees		*HH, HV*	10, 15, 20	5, 10, 20	0–105
113 (1982) 114 (1984)	Georgia Institute of Technology (EES)	Ewell, Zehner	Sea (0.9-m, 1.2–1.8-m waveheights)	9.38 GHz	*VV, HH*	~ 0	~ 0	90–160
115 (1988)	University of Michigan (Department of Electrical Engineering and Computer Science)	Ulaby et al.	Visually smooth sand	35 GHz	*VV, HH VH, HV*	24	24	0–170
			Visually smooth sand	35 GHz	*VV, HH*	30	30	0–170
			Rough sand		*VH, HV*	30	10–90	0–90
			Gravel					

*Measured and interpolated data ranges.

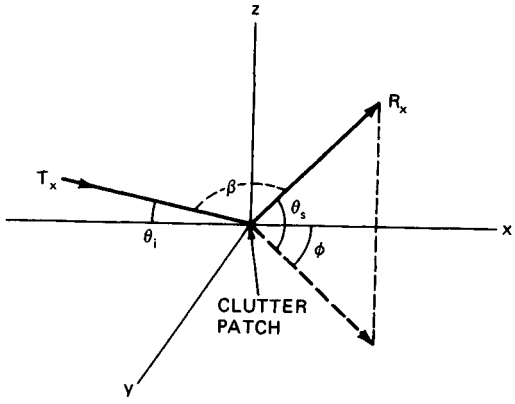

FIG. 25.9 Coordinate system for bistatic clutter measurements. θ_i = incident angle (in xz plane); θ_s = scattering angle (in plane containing z axis); ϕ = out-of-plane angle (in xy plane).

Two measurement sets are of interest: in plane, where $\phi = 180°$, and out of plane, where $\phi < 180°$. When $\phi = 180°$, $\beta = \theta_s - \theta_i$. In the monostatic case $\beta = 0$ and $\theta_s = \theta_i$ with $\phi = 180°$. Most of the data is taken at X band, with the most substantial in-plane database provided by Domville.[108–110] Because the database is sparse, mean values for $\sigma_B{}^0$ are usually given, with occasional standard deviations and probability distributions calculated.

In-Plane Land Clutter Scattering Coefficient. Figure 25.10 is a plot of Domville's X-band, vertically polarized data summary for rural land, consisting of open grassland, trees, and buildings.[108] Domville reports that since the data was a composite of different sources and averaged over different terrain conditions, differences of 10 dB in the values sometimes occurred. The spread in raw data within any data set ranged from 1 dB to 4.5 dB, however. The measured database consists of points near the lines $\theta_i = \theta_s$, $\theta_i = 90°$, and $\theta_s = 90°$ and of points along the specular ridge near the forward-scatter region. The remaining data points are interpolations.

Domville also summarized in-plane data for forest and urban areas.[108] The shape of constant $\sigma_B{}^0$ contours for all Domville's terrain types are similar. For urban areas $\sigma_B{}^0$ is generally 3 to 6 dB higher. The extent of the specular ridge is smaller, however. Because forest terrain is a more uniform scatterer, the cones extend into the forward quadrant ($\theta_s > 90°$). The ridge extent is smaller and its magnitude is about 16 dB below that of rural land. Other values of $\sigma_B{}^0$ for forest terrain are similar to those of rural land for $\theta_s < 90°$.

Domville reports[109] that at low θ_i no significant variation in $\sigma_B{}^0$ was observed for rural and forest terrain when measured at a small out-of-plane angle, $\phi = 165°$. Also at low θ_i no significant variation between horizontal, vertical, and crossed polarizations was observed for rural and forest terrain.

For semidesert, $\sigma_B{}^0$ was measured[110] at -40 dB for both horizontal and vertical polarization at $\theta_i < \sim 1°$ and for all $\theta_s > \sim 1°$. Crossed-polarization measurements were 5 to 10 dB lower. Also, $\sigma_B{}^0$ is reduced by about 0.3 dB/° as ϕ moves from 180 to 165°.

Although terrain conditions are different, the Cost in-plane data[42] matches the

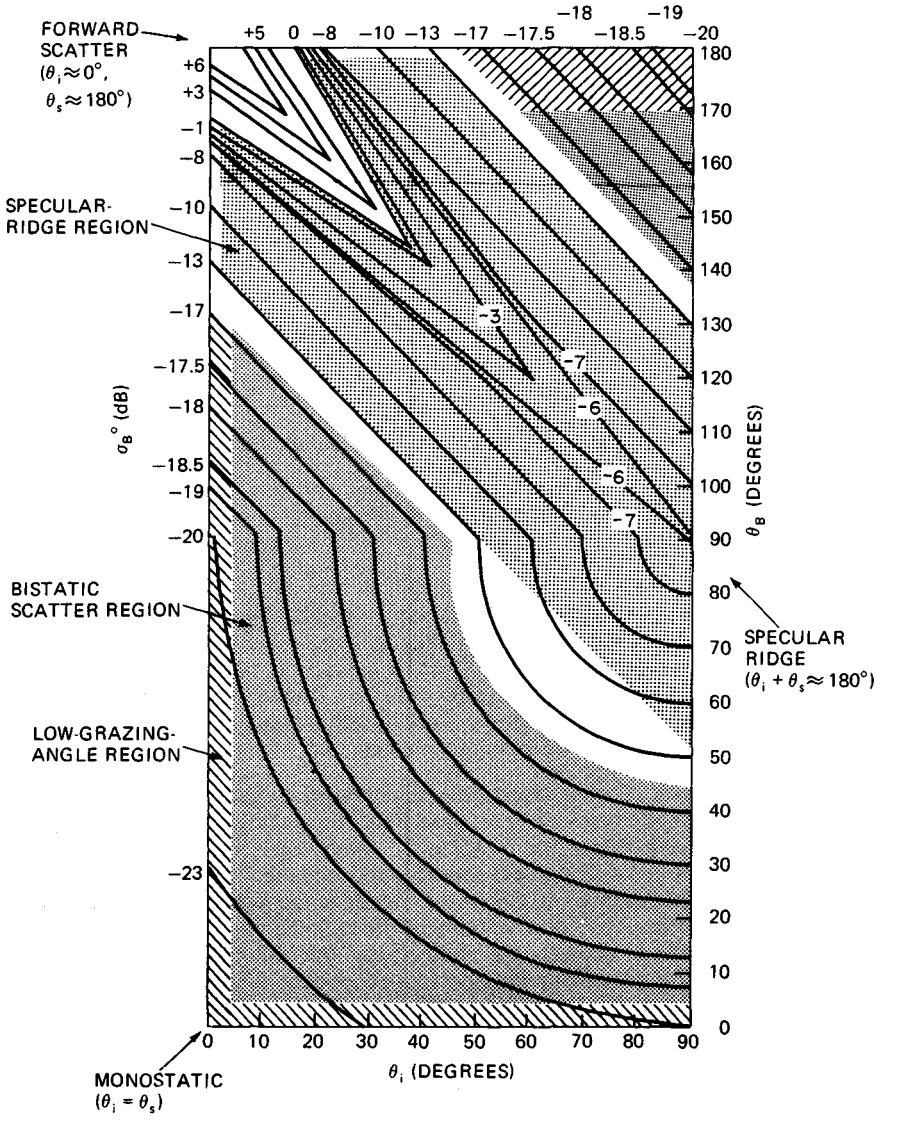

FIG. 25.10 X-band, vertically polarized, σ_B^0, in-plane ($\phi = 180°$) data summary for rural land.[108]

Domville data[108] within about 10 dB. The Cost data curves do not always approach the bistatic specular ridge monotonically even though the terrain conditions appear to be more uniform.

The in-plane Domville land clutter data can be divided into three regions: a low-grazing-angle region, where $\theta_i < \sim 3°$ or $\theta_s < \sim 3°$, the hatched area in Fig. 25.10; a specular-ridge region, where $140° \leq (\theta_i + \theta_s) \leq 220°$, the dotted area; and

a bistatic scatter region, where (θ_i, θ_s) assume values shown as the shaded areas in Fig. 25.10. Each region can be modeled, by a *semiempirical process* (containing arbitrary constants that are adjusted to fit empirical data), as follows.

The low-grazing-angle and bistatic scatter regions are based on the constant-γ monostatic clutter model:

$$\sigma_M{}^0 = \gamma \sin \theta_i \tag{25.20}$$

where $\sigma_M{}^0$ is the monostatic scattering coefficient, θ_i is the monostatic, or incident, angle on Fig. 25.9, and γ is a normalized reflectivity parameter. For farmland $\gamma \approx -15$ dB, and for wooded hills $\gamma \approx -10$ dB.[123]

The constant-γ bistatic-scatter-region model is developed by using a variation of the monostatic-bistatic equivalence theorem (Sec. 25.8), where $\sin \theta_i$ is replaced by the geometric mean of the sines of the incident and scattering angles, $(\sin \theta_i \sin \theta_s)^{1/2}$, in Eq. (25.20).[123] Hence

$$(\sigma_B{}^0)_b = \gamma (\sin \theta_i \sin \theta_s)^{1/2} \tag{25.21}$$

where $(\sigma_B{}^0)_b$ is the scattering coefficient in the bistatic scatter region. Now γ can be estimated from Fig. 25.10 by using monostatic data, which is plotted along the line $\theta_i = \theta_s$. A value of $\gamma = -16$ dB in Eq. (25.20) fits the monostatic data within about 2 dB. Using $\gamma = -16$ dB in Eq. (25.21) yields a match within 3 dB to the bistatic data, including the small triangle in the forward quadrant.

The low-grazing-angle region is modeled by the sine of the arithmetic mean of the incident and scattering angles, $\sin [(\theta_i + \theta_s)/2]$. Hence

$$(\sigma_B{}^0)_1 = \gamma \sin [(\theta_i + \theta_s)/2] \tag{25.22}$$

where $(\sigma_B{}^0)_1$ is the scattering coefficient in the low-grazing-angle region. The data match is again ~3 dB for $\gamma = -16$ dB, including the small quadrilateral in the upper right corner of Fig. 25.10. Since $(\theta_i + \theta_s)/2 = \theta_i + \beta/2$, Eq. (25.22) is an exact application of the monostatic-bistatic equivalence theorem. For very low grazing angles (θ_i or $\theta_s << \sim 1°$), but excluding the specular-ridge region, the calculations for $(\sigma_B{}^0)_1$ must be multiplied by the pattern propagation factors $F_T{}^2$ and $F_R{}^2$ and the loss terms L_T and L_R.[123]

The specular-ridge region is modeled for values of $(\sigma_B{}^0)_s \leq 1$ by a variation of the Beckman and Spizzichino theory of forward scattering from rough surfaces:[124,125]

$$(\sigma_B{}^0)_s = \exp [- (\beta_c/\sigma_s)^2] \tag{25.23}$$

where $(\sigma_B{}^0)_s$ = scattering coefficient in the specular-ridge region
σ_s = rms surface slope
β_c = angle between vertical and the bistatic bisector of θ_i and θ_s
= $|90 - (\theta_i + \theta_s)/2|$

For flat terrain $\sigma_s \approx 0.1$ rad. With a value of $\sigma_s = 0.17$ rad, Eq. (25.23) matches the specular ridge in Fig. 25.10 within 5 dB, for $(\sigma_B{}^0)_s \leq 1$.

In-Plane Sea Clutter Scattering Coefficient. Limited in-plane sea clutter measurements have been taken.[43,107,109] The Domville data[109] contains a broad range of θ_i, θ_s measurement conditions but unfortunately estimates only wind conditions and not sea state. For vertical polarization, the Domville X-band data[109] and the Pidgeon C-band data[43] show spreads of about 10 dB, and their averages match within ±5 dB. For horizontal polarization, the Domville X-band data[109] and the Pidgeon X-band data[107] again show spreads of about 10 dB, but the match is only about ±10 dB.

In view of the limited database and the uncertainties in some of the measurement conditions, caution must be exercised in modeling this data. An approximate model is the direct application of the constant-γ monostatic clutter model, Eq. (25.20), when either θ_i or θ_s is held constant. Then for the region θ_i, $\theta_s > \sim 2°$ and $\theta_i + \theta_s < \sim 100°$, $\gamma = -20$ dB matches the available vertically polarized data within about 5 dB for a 20-kn wind (≈ sea state 3 when fully developed).

Below about 2°, pattern propagation factors and losses affect the measurements. Values for $\sigma_B{}^0$ of −50 dB ±5 dB have been measured.[43] When the pattern propagation factors and losses are included in measurements, the data is sometimes called effective $\sigma_B{}^0$.[114] For $\theta_i + \theta_s > \sim 100°$, $\sigma_B{}^0 > 0$ dB, reaching +10 dB in the specular-ridge region. For horizontal polarization $\sigma_B{}^0$ is typically 1 to 5 dB lower,[109] but this difference is not significant compared with the data spread. Measured cross-polarized (*VH*) values for $\sigma_B{}^0$ are 10 to 15 dB lower than those for copolarized (*VV*) values at $\theta_i < 1°$ but only 5 to 8 dB lower at $\theta_i \approx 3°$.[43]

Out-of-Plane Scattering Coefficient. Limited out-of-plane land clutter measurements have been taken.[42,111,112,115] The Cost[42] and Ulaby[115] data shows reasonable correlation but only limited correlation with the Larson[111,112] data. There does not appear to be a satisfactory model of the available data.

However, general trends are apparent for all polarizations. First, $\sigma_B{}^0$ usually approaches a minimum as ϕ approaches 90°, with values 10 to 20 dB below the monostatic value ($\theta_i = \theta_s$, $\phi = 180°$). Second, out-of-plane $\sigma_B{}^0$ values are not significantly different (within ~ 5 dB) from in-plane $\sigma_B{}^0$ values for $\phi < \sim 10°$ and $\phi > \sim 140°$, i.e., angles close to in-plane conditions. The $\phi < \sim 10°$ limit is based on Cost, Ulaby, and Domville data; the $\phi > \sim 140°$ limit, on Ulaby and Larson data.

Ewell[113,114] measured horizontally and vertically polarized out-of-plane $\sigma_B{}^0$ for sea clutter at θ_i and θ_s near grazing incidence (θ_i, $\theta_s << 1°$). Visual estimates of sea conditions ranged from 0.9- to 1.8-m waveheight. Ratios of bistatic to monostatic scattering coefficients (median values) were calculated, with bistatic angles, $\beta \approx 180° - \phi$, ranging from 23° to 85°. The data implicitly included pattern propagation factors and losses. Since antenna heights were different, F_T, F_R, L_T, and L_R are expected to be different but were not measured. In all cases the measured bistatic to monostatic ratios were less than unity. In two cases they ranged from −2 dB to −12 dB, and in the third case they dropped from ~ −5 dB at $\beta = 23°$ to −20 to −25 dB at $\beta = 60°$. The trend was generally downward as β increased. Values for horizontal and vertical polarization showed no significant differences. For the most part both monostatic and bistatic data exhibited nearly log-normal amplitude distributions.

25.9 SPECIAL TECHNIQUES, PROBLEMS, AND REQUIREMENTS

Pulse Chasing.[49,73,126,127,129] The concept of pulse chasing has been proposed as a means to reduce the complexity and cost of multibeam bistatic

receivers, which are one solution to the beam scan-on-scan problem. The simplest pulse-chasing concept replaces the multibeam receive system (n beams, receivers, and signal processors) with a single beam, receiver, and signal processor. As shown in Fig. 25.11, the single receive beam rapidly scans the volume covered by the transmit beam, essentially chasing the pulse as it propagates from the transmitter: hence the term *pulse chasing*. In addition to the usual requirements for solving the bistatic triangle, pulse chasing requires knowledge of θ_T and pulse transmission time,[126] which can be provided to the receive site by a data link. Alternatively, if the transmit beam scan rate and the pulse repetition frequency (PRF) are uniform, the receive site can estimate these parameters as the transmit beam passes by the receive site.[127]

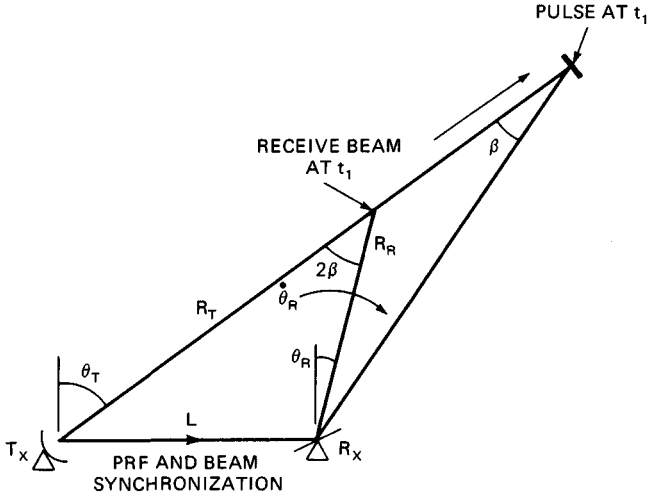

FIG. 25.11 Pulse chasing for the single-beam, continuous-scan case.

The receive beam-scanning rate must be at the transmitter's pulse propagation rate, modified by the usual geometric conditions. This rate, $\dot{\theta}_R$, is given by[73]

$$\dot{\theta}_R = c \tan (\beta/2)/R_R \tag{25.24}$$

For typical geometries $\dot{\theta}_R$ can vary from 1°/μs to 0.01°/μs. These rates and rate changes require an inertialess antenna such as a phased array and fast diode phase shifters. Normally a phased array antenna used for surveillance is programmed to switch beams in increments of a beamwidth. Fractional shifts of a beamwidth can be achieved by changing the phase of a few (symmetric) pairs of phase shifters in the array. In this way a pseudo-continuous beam scan can be generated, with the required rates and rate changes.[128]

Because of pulse propagation delays from the target to the receiver, the pointing angle of the receive beam θ_R must lag the actual pulse position. For an instantaneous pulse position that generates a bistatic angle β, $\theta_R = \theta_T - 2\beta$. In terms of the bistatic triangle, the required receive beam-pointing angle is[73]

$$\theta_R = \theta_T - 2\tan^{-1}\left(\frac{L\cos\theta_T}{R_T + R_R - L\sin\theta_T}\right) \tag{25.25}$$

The minimum receive beamwidth $(\Delta\theta_R)_m$ required to capture all returns from a range cell intersecting the common beam area is approximated by[73]

$$(\Delta\theta_R)_m \simeq (c\tau_u \tan(\beta/2) + \Delta\theta_T R_T)/R_R \tag{25.26}$$

where τ_u is the uncompressed pulse width. The approximation assumes that respective rays from the transmit and receive beams are parallel. The approximation is reasonable when $(R_T + R_R) >> L$ or when $L >> c\tau_u$.

Other implementations of pulse chasing are possible. In one concept the n-beam receive antenna is retained and two receiver–signal processors (RSPs) are time-multiplexed across the n beams. One RSP steps across the even-numbered beams, and the other RSP steps across the odd-numbered beams, so that returns in beam pairs are processed simultaneously: (1,2), (2,3), (3,4), etc. This *leapfrog* sequence is required to capture all returns in the common-beam area.

A second concept uses two beams and two RSPs step-scanning over the volume covered by the n-beam antenna. It uses an identical leapfrog sequence. Both concepts relax the fractional beam scan requirements by either sampling or stepping the beams in units of a beamwidth. Since they both process returns across two beamwidths before switching, the beam dwell time T_b is approximately $2(\Delta\theta_R)_m R_R/c$ and the stepping rate is T_b^{-1}. The approximation assumes negligible phase-shift delays and settling times.

Beam Scan on Scan. If high-gain scanning antennas are used by both the transmitter and the receiver in a bistatic surveillance radar, inefficient use is made of the radar energy, since only the volume common to both beams (the bistatic footprint) can be observed at any given time. Targets illuminated by the transmit beam outside the footprint are lost to the receiver. Four remedies to the beam scan-on-scan problem are possible: (1) fix the transmit beam for the time required to complete a surveillance frame by the receive beam, step the transmit beam one beamwidth and complete a second surveillance frame, and so forth until the transmit beam has stepped across the surveillance sector; (2) scan the transmit beam and use multiple simultaneous receive beams to cover the surveillance sector; (3) scan the transmit beam and chase the transmitted pulse with the receiver beam; and (4) broaden the transmit beamwidth to floodlight the surveillance sector, and scan the receive beam across the surveillance sector. The first and fourth remedies require a dedicated transmitter; the second and third do not.

The step-scan transmitter remedy increases the surveillance frame time by the number of required transmit beam steps. This increase is usually not acceptable for surveillance operations, and as a consequence the remedy is seldom considered. The multibeam-receiver remedy restores the frame time but increases receiver cost and complexity, since a multiple-beam antenna is required and an RSP must be used for each beam. The pulse-chasing remedy can remove requirements for multiple beams and RSPs, but at the penalty of using an inertialess (phased array) antenna with both complex and precise beam scheduling and/or multiplexing requirements, depending upon the configuration. The floodlight transmitter remedy removes all these complexities. It has the benefits of increasing data rates and simultaneously servicing multiple receivers. It incurs the pen-

alty of a reduced S/N, directly as G_T is reduced; it also suffers increased sidelobe clutter levels. In short, there are no simple and inexpensive remedies to the beam scan-on-scan problem without suffering a penalty in surveillance performance.

Sidelobe Clutter. As with a monostatic radar, a bistatic radar must contend with sidelobe clutter. When both transmitter and receiver are ground-based and separated by a baseline range L, only ground clutter from regions having an adequate line of sight (LOS) to both the transmitter and the receiver will enter the receiver antenna sidelobes. That region is defined for a smooth earth as the common-coverage area A_C. From Eqs. (25.9), (25.10), and (25.12), when $h_t = 0$ and $L \geq r_R + r_T = 130\ (\sqrt{h_R} + \sqrt{h_T})$, A_C for ground clutter is zero, and no sidelobe (or main-lobe) clutter enters the receive antenna. Targets with adequate LOS to both transmitter and receiver can be detected in a thermal-noise-limited background. This situation is analogous to a monostatic radar detecting targets at ranges greater than r_T.

This development applies to ocean scenarios but seldom is valid for land scenarios. In land scenarios variable terrain can decrease clutter levels by masking a clutter LOS when $L < r_R + r_T$ or increase clutter levels by generating a clutter LOS when $L > r_R + r_T$.

When the transmitter and/or the receiver is elevated or airborne, LOS restrictions are greatly reduced but not necessarily eliminated. Two clutter problems unique to bistatic radars are encountered in this situation. The first occurs when a floodlight transmit beam is used. To a first order, sidelobe clutter levels are reduced only by the one-way receive antenna sidelobes, in contrast to two-way sidelobe clutter reduction for a monostatic radar.

The second problem occurs when the transmitter and/or the receiver are moving, e.g., when airborne. Now the bistatic clutter doppler returns skew and spread, depending upon the geometry for each clutter patch and the kinematics of the transmit and receive platforms. Doppler skew is defined in terms of isodoppler contours, or isodops, given by Eq. (25.18) for two dimensions and a flat earth. The skew is range- and angle-dependent. The range-dependent skewing effect is not present in an airborne monostatic radar. Clutter spread in a particular sidelobe range cell is centered on the doppler skew present in the range cell.

These skewing and spreading effects, along with increased clutter levels, can greatly complicate the ability of a bistatic radar to detect targets in clutter. Remedies include conventional doppler filtering and high time-bandwidth waveforms; the judicious use of masking when available; control of the geometry, especially when a dedicated or cooperative transmitter is available; design of very low receive (and transmit when possible) antenna sidelobe levels; sidelobe blanking of discrete clutter returns; range or range-doppler averaging in the constant false-alarm rate (CFAR) unit for homogeneous clutter; and spatial excision of clutter returns. One implementation of this last technique relies on knowledge of the geometry and kinematics to predict the clutter doppler and spread in a given area. Then a filter or gate is set to excise main-beam clutter returns in that area. The amount of range-doppler space excised by this procedure can be as high as 8 percent.[45]

Time Synchronization. Time synchronization is required between the bistatic transmitter and receiver for range measurement. Timing accuracies on the order of a fraction of the transmitter's (compressed) pulse width are typically desired over the duration of an operation. Time synchronization can be accomplished directly by receiving a signal from the transmitter, demodulating the signal if necessary, and using the demodulated signal to

synchronize a clock in the receiver. The transmitter signal can be sent via landline, via a communication link, or directly at the transmitter's RF if an adequate line of sight (LOS) exists between transmitter and receiver. If an adequate LOS is not available, it can be sent via a scatter path, where the scatterer has adequate LOS to both the transmitter and the receiver.[49] In this case, the scatterer must lie in the common-coverage area, as defined by Eq. (25.12). Transmission via tropospheric scatter can also be used in special cases.[50] In all these direct time synchronization schemes, implementation is straightforward, much like the initial synchronization process in communication systems. They can also be used for any type of transmitter pulse repetition interval (PRI) modulation: stable, staggered, jittered, and random. With time synchronization established, target range is calculated via Eq. (25.7) or similar methods.

For stable PRIs, time synchronization can be accomplished indirectly by using identical stable clocks at the transmitter and receiver sites. The clocks can be synchronized periodically, for example, whenever the transmitter and receiver are within LOS or located together if one or both are mobile. Direct time synchronization methods can be used for this task. Alternatively, the stable clocks can be slaved to a second source, such as Navstar GPS or loran C.[50,82,130] Indirect time synchronization can also be employed with a dedicated or cooperative transmitter using random PRIs if a random code sequence is established a priori and is known by the receive site.

In direct time synchronization, the required clock stability between updates is, to a first order, $\Delta\tau/T_u$, where $\Delta\tau$ is the required timing accuracy and T_u is the clock update interval. The update interval typically ranges from a minimum of the transmitter's interpulse period to a maximum of the transmitter's antenna scan period. The former usually requires a dedicated link between transmitter and receiver; the latter can be implemented whenever the transmit beam scans past the receive site, given an adequate LOS, and is sometimes called *direct breakthrough*.[130] Temperature-controlled crystal oscillators can often satisfy these requirements.

However, when direct-breakthrough time synchronization is used, multipath and other propagation anomalies, as well as radio-frequency interference (RFI), will degrade the accuracy of updating. Errors of ± 1 μs have been measured when a direct LOS is available.[131] They increase to ± 5 μs over a tropospheric propagation path.[130]

Since two clocks are used in indirect time synchronization, clock stability is, to a first order, $\Delta\tau/2T_u$. For T_u on the order of hours, atomic clocks are usually required to satisfy this requirement. Temperature-controlled crystal oscillators, an integral part of atomic clocks, will usually satisfy short-term (< 1 s) stability requirements. If the stable clocks are slaved to a second source, estimated timing accuracies of 0.5 μs for loran-C and <0.1 μs for Navstar GPS are reported.[82]

Phase Synchronization and Stability. As with monostatic radars, doppler or MTI processing can be used by the bistatic receiver to reject clutter or chaff. If noncoherent MTI is acceptable for clutter rejection, the bistatic receiver can use a clutter reference, exactly as a monostatic radar would, given that clutter patches are illuminated by the transmitter.

In one bistatic noncoherent MTI implementation, called *phase priming*, an oscillator at the receiver was phase-synchronized at the PRF rate with a small sample of close-in clutter returns.[132] Phase coherence was obtained within about 10 μs and extended over 1 ms. The process was found insensitive to the clutter signal level but quite sensitive to pulse-to-pulse phase fluctuations in the clutter signal.

If coherent processing is required, phase synchronization can be established with methods similar to those used for time synchronization: directly by phase-locking the receiver to the transmit signal or indirectly by using identical stable clocks in the transmitter and the receiver. Phase accuracy, or stability, requirements are the same as those for coherent processing by a monostatic radar: from 0.01λ to 0.1λ, or 3.6° to 36° of RF phase over a coherent processing interval,[133] with 0.01λ representing more typical design requirements.

Direct phase locking can be implemented as in direct time synchronization: via landline, communication link, or at the transmitter's RF. If a direct RF link is used, adequate transmitter-to-receiver LOS is again required. It is also subject to multipath and to phase reversals if coherent operation is required across transmitter antenna sidelobes. However, this latter problem can be overcome by a Costas loop for phase reversals near 180°.[134] An extension of direct-path phase locking is the use of the direct-path signal as a reference signal in a correlation processor.[135]

For direct-path phase locking, clock stability is $\Delta\phi/2\pi f\Delta T$, where $\Delta\phi$ is the allowable rms sinusoidal phase error, f is the transmitter frequency, and ΔT is the difference in propagation time between the transmitter-target-receiver path and the transmitter-receiver (direct) path.[133] As with time synchronization, this requirement can usually be satisfied by a temperature-controlled crystal oscillator.

For matched stable clocks in the transmitter and receiver, phase stability is usually required over a coherent processing time T. Thus clock stability is $\Delta\phi/2\pi fT$. Again, atomic clocks are usually required, with crystal oscillators used for short-term stability. However, when $T < \sim 1$ s, integral crystal oscillators are usually acceptable. Quadratic phase errors caused by long-term drift in the stable clocks are usually smaller than allowable short-term sinusodial phase errors and can often be ignored.

In most types of SAR images, the integrated sidelobe ratio (ISLR) is an important criterion for image quality. It is a measure of the energy from a particular target that appears at image locations other than that corresponding to the target. Typically a −30- to −40-dB ISLR allocation for clock, or stable local oscillator (stalo), phase noise is desired.[53] When a single stalo is used, as in the monostatic case, these levels can be achieved for long coherent integration terms ($T > 10$ s) since low-frequency components of the phase noise are partially canceled in the demodulation process. However, since both bistatic phase synchronization techniques use two stalos, these low-frequency components do not cancel, resulting in higher ISLRs. Thus the bistatic SAR image quality, in terms of doppler or azimuth sidelobes, is degraded for coherent integration times greater than about 1 s at X band[53] unless very-high-quality clocks are used.

When direct-path phase locking is used by a bistatic SAR, the required motion-compensation phase shift (to track the target phase) must correct for relative motion between transmitter and receiver. When matched stable clocks are used, this correction is not required.[133]

Either time or phase errors can dominate synchronization requirements, depending upon the range and doppler accuracies needed. While all these requirements usually can be met, implementation is more complicated, time-consuming, and costly when compared with a monostatic system, which uses one clock for both time and phase synchronization.

REFERENCES

1. Skolnik, M. I.: "Introduction to Radar Systems," McGraw-Hill Book Company, New York, 1980.
2. *Microwave Syst. News Commun. Technol.*, vol. 18, p. 60, February 1988.
3. Heimiller, R. C., J. E. Belyea, and P. G. Tomlinson: Distributed Array Radar, *IEEE Trans.*, vol. AES-19, pp. 831–839, 1983.
4. Steinberg, B. D.: "Principles of Aperture and Array System Design—Including Random and Adaptive Arrays," John Wiley & Sons, New York, 1976.
5. Steinberg, B. D., and E. Yadin: Distributed Airborne Array Concepts, *IEEE Trans.*, vol. AES-18, pp. 219–226, 1982.
6. Steinberg, B. D.: High Angular Microwave Resolution from Distorted Arrays, *Proc. Int. Comput. Conf.*, vol. 23, 1980.
7. Easton, R. L., and J. J. Fleming: The Navy Space Surveillance System, *Proc. IRE*, vol. 48, pp. 663–669, 1960.
8. Mengel, J. T.: Tracking the Earth Satellite, and Data Transmission by Radio, *Proc. IRE*, vol. 44, pp. 755–760, June 1956.
9. Merters, L. E., and R. H. Tabeling: Tracking Instrumentation and Accuracy on the Eastern Test Range, *IEEE Trans.*, vol. SET-11, pp. 14–23, March 1965.
10. Scavullo, J. J., and F. J. Paul, "Aerospace Ranges: Instrumentation," D. Van Nostrand Company, Princeton, N.J., 1965.
11. Steinberg, B. D., et al.: First Experimental Results for the Valley Forge Radio Camera Program, *Proc. IEEE*, vol. 67, pp. 1370–1371, September 1979.
12. Steinberg, B. D.: Radar Imaging from a Distributed Array: The Radio Camera Algorithm and Experiments, *IEEE Trans.*, vol. AP-29, pp. 740–748, September 1981.
13. Salah, J. E., and J. E. Morriello: Development of a Multistatic Measurement System, *IEEE Int. Radar Conf.*, pp. 88–93, 1980.
14. Multistatic Mode Raises Radar Accuracy, *Aviat. Week Space Technol.*, pp. 62–69, July 14, 1980.
15. Skolnik, M. I.: An Analysis of Bistatic Radar, *IRE Trans.*, vol. ANE-8, pp. 19–27, March 1961.
16. Caspers, J. M.: Bistatic and Multistatic Radar, chap. 36 in Skolnik, M. I. (ed.): "Radar Handbook," McGraw-Hill Book Company, New York, 1970.
17. Ewing, E. F.: The Applicability of Bistatic Radar to Short Range Surveillance, *IEE Conf. Radar 77, Publ.* 155, pp. 53–58, London, 1977.
18. Ewing, E. F., and L. W. Dicken: Some Applications of Bistatic and Multi-Bistatic Radars, *Int. Radar Conf.*, pp. 222–231, Paris, 1978.
19. Farina, A., and E. Hanle: Position Accuracy in Netted Monostatic and Bistatic Radar, *IEEE Trans.*, vol. AES-19, pp. 513–520, July 1983.
20. Hanle, E.: Survey of Bistatic and Multistatic Radar, *Proc. IEE*, vol. 133, pt. F, pp. 587–595, December 1986.
21. Taylor, A. H., L. C. Young, and L. A. Hyland: U.S. Patent 1,981,884, System for Detecting Objects by Radio, Nov. 27, 1934.
22. Williams, A. F.: The Study of Radar, "Research Science and Its Application in Industry," vol. 6, Butterworth Scientific Publications, London, 1953, pp. 434–440.
23. Watson-Watt, Sir R.: "The Pulse of Radar," Dial Press, New York, 1959.
24. Skolnik, M. I.: Fifty Years of Radar, *Proc. IEEE*, vol. 73, pp. 182–197, February 1985.

25. Guerlac, H. E.: "Radar in World War II," vols. I and II, Tomask/American Institute of Physics, New York, 1987.

26. Price, A.: "The History of US Electronic Warfare," vol. 1, The Association of Old Crows, 1984.

27. Barton, D. K.: Historical Perspective on Radar, *Microwave J.*, vol. 23, p. 21, August 1980.

28. Summers, J. E., and D. J. Browning: An Introduction to Airborne Bistatic Radar, *IEE Colloq. Ground Airborne Multistatic Radar*, pp. 2/1–2/5, London, 1981.

29. Eon, L. G.: An Investigation of the Techniques Designed to Provide Early Warning Radar Fence for the Air Defense of Canada, *Defense Research Board (Canada), Rept. TELS* 100, Dec. 1, 1952.

30. Sloane, E. A., J. Salerno, E. S. Candidas, and M. I. Skolnik: A Bistatic CW Radar, *MIT Lincoln Laboratory Tech. Rept.* 82, *AD* 76454, Lexington, Mass., June 6, 1955.

31. Skolnik, M. I., J. Salerno, and E. S. Candidas: Prediction of Bistatic CW Radar Performance, *Symp. Radar Detection Theory, ONR Symp. Rept. ACR*-10, pp. 267–278, Washington, Mar. 1–2, 1956.

32. Skolnik, M. I.: private communication, September 1986.

33. Siegel, K. M., et al.: Bistatic Radar Cross Sections of Surfaces of Revolution, *J. Appl. Phys.*, vol. 26, pp. 297–305, March 1955.

34. Siegel, K. M.: Bistatic Radars and Forward Scattering, *Proc. Nat. Conf. Aeronaut. Electron.*, pp. 286–290, May 12–14, 1958.

35. Schultz, F. V., et al.: Measurement of the Radar Cross-Section of a Man, *Proc. IRE*, vol. 46, pp. 476–481, February 1958.

36. Crispin, J. W., Jr., et al.: "A Theoretical Method for the Calculation of Radar Cross Section of Aircraft and Missiles," *University of Michigan, Radiation Lab. Rept.* 2591-1-*H*, July 1959.

37. Hiatt, R. E., et al.: Forward Scattering by Coated Objects Illuminated by Short Wavelength Radar, *Proc. IRE*, vol. 48, pp. 1630–1635, September 1960.

38. Garbacz, R. J., and D. L. Moffett: An Experimental Study of Bistatic Scattering from Some Small, Absorber-Coated, Metal Shapes, *Proc. IRE*, vol. 49, pp. 1184–1192, July 1961.

39. Andreasen, M. G.: Scattering from Bodies of Revolution, *IEEE Trans.*, vol. AP-13, pp. 303–310, March 1965.

40. Mullin, C. R., et al.: A Numerical Technique for the Determination of the Scattering Cross Sections of Infinite Cylinders of Arbitrary Geometric Cross Section, *IEEE Trans.*, vol. AP-13, pp. 141–149, January 1965.

41. Kell, R. E.: On the Derivation of Bistatic RCS from Monostatic Measurements, *Proc. IEEE*, vol. 53, pp. 983–988, August 1965.

42. Cost, S. T.: "Measurements of the Bistatic Echo Area of Terrain of X-Band," *Ohio State University, Antenna Lab. Rept.* 1822-2, May 1965.

43. Pidgeon, V. W.: Bistatic Cross Section of the Sea, *IEEE Trans.*, vol. AP-14, pp. 405–406, May 1966.

44. Lefevre, R. J.: Bistatic Radar: New Application for an Old Technique, *WESCON Conf. Rec.*, pp. 1–20, San Francisco, 1979.

45. Fleming, F. L., and N. J. Willis: Sanctuary Radar, *Proc. Mil. Microwaves Conf.*, pp. 103–108, London, Oct. 22–24, 1980.

46. Forrest, J. R., and J. G. Schoenenberger: Totally Independent Bistatic Radar Receiver with Real-Time Microprocessor Scan Correction, *IEEE Int. Radar Conf.*, pp. 380–386, 1980.

47. Pell, C., et al.: An Experimental Bistatic Radar Trials System, *IEE Colloq. Ground Airborne Multistatic Radar*, pp. 6/1–6/12, London, 1981.

48. Schoenenberger, J. G., and J. R. Forrest: Principles of Independent Receivers for Use with Co-operative Radar Transmitters, *Radio Electron. Eng.*, vol. 52, pp. 93–101, February 1982.

49. Soame, T. A., and D. M. Gould: Description of an Experimental Bistatic Radar System, *IEE Int. Radar Conf. Publ.* 281, pp. 12–16, 1987.

50. Dunsmore, M. R. B.: Bistatic Radars for Air Defense, *IEE Int. Radar Conf. Publ.* 281, pp. 7–11, 1987.

51. Lorti, D. C., and M. Balser, Simulated Performance of a Tactical Bistatic Radar System, *IEEE EASCON 77 Rec. Publ. 77 CH*1255-9, pp. 4-4A–4-40, Arlington, Va., 1977.

52. Tactical Bistatic Radar Demonstrated, *Def. Electron.*, no. 12, pp. 78–82, 1980.

53. Auterman, J. L.: Phase Stability Requirements for a Bistatic SAR, *Proc. IEEE Nat. Radar Conf.*, pp. 48–52, Atlanta, March 1984.

54. Bistatic Radars Hold Promise for Future Systems, *Microwave Syst. News*, pp. 119–136, October 1984.

55. Griffiths, H. D., et al.: Television-Based Bistatic Radar, *Proc. IEE*, vol. 133, pt. F, pp. 649–657, December 1986.

56. Tomiyasu, K., Bistatic Synthetic Aperture Radar Using Two Satellites, *IEEE EASCON Rec.*, pp. 106–110, Arlington, Va., 1978.

57. Lee, P. K., and T. F. Coffey: Space-Based Bistatic Radar: Opportunity for Future Tactical Air Surveillance, *IEEE Int. Radar Conf.*, pp. 322–329, Washington, 1985.

58. Hsu, Y. S., and D. C. Lorti: Spaceborne Bistatic Radar—An Overview, *Proc. IEE*, vol. 133, pt. F, pp. 642–648, December 1986.

59. Anthony, S., et al.: Calibration Considerations in a Large Bistatic Angle Airborne Radar System for Ground Clutter Measurements, *Proc. IEEE Nat. Radar Conf.*, pp. 230–234, Ann Arbor, Mich., Apr. 20, 1988.

60. Walker, B. C., and M. W. Callahan: A Bistatic Pulse-Doppler Intruder-Detection Radar, *IEEE Int. Radar Conf.*, pp. 130–134, 1985.

61. Dawson, C. H.: Inactive Doppler Acquisition Systems, *Trans. AIEE*, vol. 81, pp. 568–571, January 1963.

62. Detlefsen, J.: Application of Multistatic Radar Principles to Short Range Imaging, *Proc. IEE*, vol. 133, pt. F, December 1986.

63. Nicholson, A. M., and G. F. Ross: A New Radar Concept for Short Range Application, *IEEE Int. Radar Conf.*, 1975.

64. Tyler, G. L.: The Bistatic Continuous-Wave Radar Method for the Study of Planetary Surfaces, *J. Geophys. Res.*, vol. 71, pp. 1559–1567, Mar. 15, 1966.

65. Tyler, G. L., et al.: Bistatic Radar Detection of Lunar Scattering Centers with Lunar Orbiter 1, *Science*, vol. 157, pp. 193–195, July 1967.

66. Pavel'yev, A. G., et al.: The Study of Venus by Means of the Bistatic Radar Method, *Radio Eng. Electron. Phys. (U.S.S.R.)*, vol. 23, October 1978.

67. Zebker, H. Z., and G. L. Tyler: Thickness of Saturn's Rings Inferred from Voyager 1 Observations of Microwave Scatter, *Science*, vol. 113, pp. 396–398, January 1984.

68. Tang, C. H., et al.: Measurements of Electrical Properties of the Martian Surface, *J. Geophys. Res.*, vol. 82, pp. 4305–4315, September 1977.

69. Zhou Zheng-Ou, et al.: A Bistatic Radar for Geological Probing, *Microwave J.*, pp. 257–263, May 1984.

70. Peterson, A. M., et al.: Bistatic Radar Observation of Long Period, Directional Ocean-Wave Spectra with Loran-A, *Science*, vol. 170, pp. 158–161, October 1970.

71. Doviak, R. J., et al.: Bistatic Radar Detection of High Altitude Clear Air Atmospheric Targets, *Radio Sci.*, vol. 7, pp. 993–1003, November 1972.

72. Wright, J. W., and R. I. Kressman: First Bistatic Oblique Incidence Ionograms Between Digital Ionosondes, *Radio Sci.*, vol. 18, pp. 608–614, July–August 1983.

73. Jackson, M. C.: The Geometry of Bistatic Radar Systems, *IEE Proc.*, vol. 133, pt. F, pp. 604–612, December 1986.

74. Davies, D. E. N.: Use of Bistatic Radar Techniques to Improve Resolution in the Vertical Plane, *IEE Electron. Lett.*, vol. 4, pp. 170–171, May 3, 1968.

75. McCall, E. G.: Bistatic Clutter in a Moving Receiver System, *RCA Rev.*, pp. 518–540, September 1969.

76. Crowder, H. A.: Ground Clutter Isodops for Coherent Bistatic Radar, *IRE Nat. Conv. Rec.*, pt. 5, pp. 88–94, New York, 1959.

77. Dana, R. A., and D. L. Knapp: The Impact of Strong Scintillation on Space Based Radar Design, I: Coherent Detection, *IEEE Trans.*, vol. AES-19, July 1983.

78. Pyati, V. P.: The Role of Circular Polarization in Bistatic Radars for Mitigation of Interference Due to Rain, *IEEE Trans.*, vol. AP-32, pp. 295–296, March 1984.

79. McCue, J. J. G.: Suppression of Range Sidelobes in Bistatic Radars, *Proc. IEEE*, vol. 68, pp. 422–423, March 1980.

80. Buchner, M. R.: A Multistatic Track Filter with Optimal Measurement Selection, *IEE Radar Conf.*, pp. 72–75, London, 1977.

81. Farina, A.: Tracking Function in Bistatic and Multistatic Radar Systems, *Proc. IEE*, vol. 133, pt. F, pp. 630–637, December 1986.

82. Retzer, G.: Some Basic Comments on Multistatic Radar Concepts and Techniques, *IEE Colloq. Ground Airborne Multistatic Radar*, pp. 3/1–3/3, London, 1981.

83. Hoisington, D. B., and C. E. Carroll: "Improved Sweep Waveform Generator for Bistatic Radar," U.S. Naval Postgraduate School, Monterey, Calif., August 1975.

84. Kuschel, H.: Bistatic Radar Coverage—A Quantification of System and Environmental Interferences, *IEE Int. Radar Conf. Publ.* 281, pp. 17–21, 1987.

85. Barrick, D. E. Normalization of Bistatic Radar Return, *Ohio State University, Res. Found. Rept.* 1388-13, Jan. 15, 1964.

86. Peake, W. H., and S. T. Cost: The Bistatic Echo Area of Terrain of 10 GHz, *WESCON 1968*, sess. 22/2, pp. 1–10.

87. Weiner, M. M., and P. D. Kaplan: Bistatic Surface Clutter Resolution Area at Small Grazing Angles, *MITRE Corporation, RADC-TR*-82-289, *AD A*123660, Bedford, Mass., November 1982.

88. Moyer, L. R., C. J. Morgan, and D. A. Rugger: An Exact Expression for the Resolution Cell Area in a Special Case of Bistatic Radar Systems, *Trans. IEEE*, vol. AES-25, July 1989.

89. Lorti, D. C., and J. J. Bowman: Will Tactical Aircraft Use Bistatic Radar?, *Microwave Syst. News*, vol. 8, pp. 49–54, September 1978.

90. Moyer, L. R. (TSC): private communication, February 1988.

91. Kock, W. I.: Related Experiments with Sound Waves and Electromagnetic Waves, *Proc. IRE*, vol. 47, pp. 1200–1201, July 1959.

92. Siegel, K. M., et al.: RCS Calculation of Simple Shapes—Bistatic, chap. 5, "Methods of Radar Cross-Section Analysis," Academic Press, New York, 1968.

93. Weil, H., et al.: Scattering of Electromagnetic Waves by Spheres, *University of Michigan, Radiat. Lab. Stud. Radar Cross Sections X, Rept.* 2255-20-*T*, contract AF 30(602)-1070, July 1956.

94. King, R. W. P., and T. T. Wu: "The Scattering and Diffraction of Waves," Harvard University Press, Cambridge, Mass., 1959.

95. Goodrich, R. F., et al.: Diffraction and Scattering by Regular Bodies—I: The Sphere, *University of Michigan, Dept. Electr. Eng. Rept.* 3648-1-*T*, 1961.

96. Matsuo, M., et al.: Bistatic Radar Cross Section Measurements by Pendulum Method, *IEEE Trans.*, vol. AP-18, pp. 83–88, January 1970.

97. Ewell, G. W., and S. P. Zehner: Bistatic Radar Cross Section of Ship Targets, *IEEE J. Ocean. Eng.*, vol. OE-5, pp. 211–215, October 1980.

98. Radar Cross-Section Measurements, *General Motors Corporation, Delco Electron. Div. Rept. R*81-152, Santa Barbara, Calif., 1981.

99. Bachman, C. G.: "Radar Targets," Lexington Books, Lexington, Mass., 1982, p. 29.

100. Paddison, F. C., et al.: Large Bistatic Angle Radar Cross Section of a Right Circular Cylinder, *Electromagnetics*, vol. 5, pp. 63–77, 1985.

101. Glaser, J. I.: Bistatic RCS of Complex Objects Near Forward Scatter, *IEEE Trans.*, vol. AES-21, pp. 70–78, January 1985.

102. Cha, Chung-Chi, et al.: An RCS Analysis of Generic Airborne Vehicles' Dependence on Frequency and Bistatic Angle, *IEEE Nat. Radar Conf.*, pp. 214–219, Ann Arbor, Mich., Apr. 20, 1988.

103. Weiner, M. M. (MITRE Corporation): private communication, April 1988.

104. Pierson, W. A., et al.: The Effect of Coupling on Monostatic-Bistatic Equivalence, *Proc. IEEE*, pp. 84–86, January 1971.

105. Barton, D. K.: "Modern Radar System Analysis," Artech House, Norwood, Mass., 1988, pp. 121–123.

106. Burk, G. J., and A. J. Foggio: "Numerical Electromagnetic Code (NEC)—Method of Moments," Naval Ocean Systems Center, San Diego, 1981.

107. Pidgeon, V. W.: Bistatic Cross Section of the Sea for Beaufort 5 Sea, *Science Technol.*, vol. 17, American Astronautical Society, San Diego, 1968, pp. 447–448.

108. Domville, A. R.: The Bistatic Reflection from Land and Sea of X-Band Radio Waves, pt. I, *GEC (Electronics) Ltd., Memo. SLM* 1802, Stanmore, England, July 1967.

109. Domville, A. R.: The Bistatic Reflection from Land and Sea of X-Band Radio Waves, pt. II, *GEC (Electronics) Ltd., Memo SLM* 2116, Stanmore, England, July 1968.

110. Domville, A. R.: The Bistatic Reflection from Land and Sea of X-Band Radio Waves, pt. II—Suppl., *GEC-AEI (Electronics) Ltd., Memo. SLM* 2116 (*Suppl.*), Stanmore, England, July 1969.

111. Larson, R. W., et al.: Bistatic Clutter Data Measurements Program, *Environmental Research Institute of Michigan, RADC-TR*-77-389, *AD*-A049037, November 1977.

112. Larson, R. W., et al.: Bistatic Clutter Measurements, *IEEE Trans.*, vol. AP-26, pp. 801–804, November 1978.

113. Ewell, G. W., and S. P. Zehner: Bistatic Sea Clutter Return Near Grazing Incidence, *IEE Radar Conf. Publ.* 216, pp. 188–192, October 1982.

114. Ewell, G. W., Bistatic Radar Cross Section Measurements, chap. 7 in Currie, N. C. (ed.): "Technology of Radar Reflectivity Measurement," Artech House, Norwood, Mass., 1984.

115. Ulaby, F. T., et al.: Millimeter-Wave Bistatic Scattering from Ground and Vegetation Targets, *IEEE Trans.*, vol. GE-26, no. 3, May 1988.

116. Nathanson, F. E., "Radar Design Principles," McGraw-Hill Book Company, New York, 1969.

117. Vander Schurr, R. E., and P. G. Tomlinson: Bistatic Clutter Analysis, *Decision-Science Applications, Inc., RADC-TR*-79-70, April 1979.

118. Sauermann, G. O., and P. C. Waterman: Scattering Modeling: Investigation of Scattering by Rough Surfaces, *MITRE Corporation, Rept. MTR*-2762, *AFAL-TR*-73-334, January 1974.

119. Zornig, J. G., et al.: Bistatic Surface Scattering Strength at Short Wavelengths, *Yale University, Dept. Eng. Appl. Sci. Rept. CS*-9, *AD*-A041316, June 1977.

120. Bramley, E. N., and S. M. Cherry: Investigation of Microwave Scattering by Tall Buildings, *Proc. IEE*, vol. 120, pp. 833–842, August 1973.

121. Brindly, A. E., et al.: A Joint Army/Air Force Investigation of Reflection Coefficient at C and K_u Bands for Vertical, Horizontal and Circular System Polarizations, *IIT Research Institute, Final Rept., TR*-76-67, *AD-A*031403, Chicago, July 1976.

122. Tang, C. H., et al.: Bistatic Radar Measurements of Electrical Properties of the Martian Surface, *J. Geophys. Res.*, vol. 82, pp. 4305–4315, September 1977.

123. Barton, D. K.: Land Clutter Models for Radar Design and Analysis, *Proc. IEEE*, vol. 73, pp. 198–204, February 1985.

124. Beckman, P., and A. Spizzichino: "The Scattering of EM Waves from Rough Surfaces," Pergamon Press, New York, 1963.

125. Nathanson, F., Technology Service Corporation: private communication, May 1988.

126. Hanle, E.: Pulse Chasing with Bistatic Radar-Combined Space-Time Filtering, in Schussler, H. W. (ed.): "Signal Processing II: Theories and Applications," Elsevier Science Publishers B.V., North Holland, pp. 665–668.

127. Schoenenberger, J. G., and J. R. Forrest: Principles of Independent Receivers for Use with Co-operative Radar Transmitters, *Radio Electron. Eng.*, vol. 52, pp. 93–101, February 1982.

128. Frank, J., and J. Ruze, Beam Steering Increments for a Phased Array, *IEEE Trans.*, vol. AP-15, pp. 820–821, November 1967.

129. Freedman, N.: Bistatic Radar System Configuration and Evaluation, *Raytheon Company, Independ. Dev. Proj.* 76*D*-220, *Final Rept. ER*76-4414, Dec. 30, 1976.

130. Bovey, C. K., and C. P. Horne, Synchronization Aspects for Bistatic Radars, *IEE Int. Radar Conf. Publ.* 281, pp. 22–25, 1987.

131. Schoenenberger, J. G., et al.: Design and Implementation of a UHF Band Bistatic Radar Receiver, *IEE Colloq. Ground Airborne Multistatic Radar*, pp. 7/1–7/3, London, 1981.

132. Griffiths, H. D., and S. M. Carter: Provision of Moving Target Indication in an Independent Bistatic Radar Receiver, *Radio Electron. Eng.*, vol. 54, pp. 336–342, July–August 1984.

133. Kirk, Jr., J. C.: Bistatic SAR Motion Compensation, *IEEE Int. Radar Conf.*, pp. 360–365, 1985.

134. Costas, J. P.: Synchronous Communications, *Proc. IRE*, vol. 44, pp. 1713–1718, December 1956.

135. Retzer, G.: A Concept for Signal Processing in Bistatic Radar, *IEEE Int. Radar Conf.*, pp. 288–293, 1980.